



























NGDEEP: The Star Formation and Ionization Properties of Galaxies at $1.7 < z < 3.4$

LU SHEN ^{1,2} CASEY PAPOVICH ^{1,2} JASLEEN MATHARU ^{3,4} NOR PIRZKAL ⁵ WEIDA HU ^{1,2}
DANIELLE A. BERG ⁶ MICAELA B. BAGLEY ⁶ BREN E. BACKHAUS ⁷ NIKKO J. CLERI ^{8,9,10}
MARK DICKINSON ¹¹ STEVEN L. FINKELSTEIN ⁶ NIMISH P. HATHI ¹² MARC HUERTAS-COMPANY ^{13,14,15}
TAYLOR A. HUTCHISON ^{16,*} MAURO GIAVALISCO ¹⁷ NORMAN A. GROGIN ¹⁸ ANNE E. JASKOT ¹⁹
INTAE JUNG ²⁰ JEYHAN S. KARTALTEPE ²¹ ANTON M. KOEKEMOER ²² JENNIFER M. LOTZ ²³
PABLO G. PÉREZ-GONZÁLEZ ²⁴ BARRY ROTHBERG ^{25,26} RAYMOND C. SIMONS ²⁷
BRITTANY N. VANDERHOOF ¹² AND L. Y. AARON YUNG ¹²

¹*Department of Physics and Astronomy, Texas A&M University, College Station, TX, 77843-4242 USA*

²*George P. and Cynthia Woods Mitchell Institute for Fundamental Physics and Astronomy, Texas A&M University, College Station, TX, 77843-4242 USA*

³*Cosmic Dawn Center (DAWN), Denmark*

⁴*Niels Bohr Institute, University of Copenhagen, Jagtvej 128, DK-2200 Copenhagen N, Denmark*

⁵*ESA/AURA Space Telescope Science Institute*

⁶*Department of Astronomy, The University of Texas at Austin, Austin, TX, USA*

⁷*Department of Physics and Astronomy, University of Kansas, Lawrence, KS 66045, USA*

⁸*Department of Astronomy and Astrophysics, The Pennsylvania State University, University Park, PA 16802, USA*

⁹*Institute for Computational and Data Sciences, The Pennsylvania State University, University Park, PA 16802, USA*

¹⁰*Institute for Gravitation and the Cosmos, The Pennsylvania State University, University Park, PA 16802, USA*

¹¹*NSF's National Optical-Infrared Astronomy Research Laboratory, 950 N. Cherry Ave., Tucson, AZ 85719, USA*

¹²*Space Telescope Science Institute, 3700 San Martin Drive, Baltimore, MD 21218, USA*

¹³*Instituto de Astrofísica de Canarias, La Laguna, Tenerife, Spain*

¹⁴*Universidad de la Laguna, La Laguna, Tenerife, Spain*

¹⁵*Université Paris-Cité, LERMA - Observatoire de Paris, PSL, Paris, France*

¹⁶*Astrophysics Science Division, NASA Goddard Space Flight Center, 8800 Greenbelt Rd, Greenbelt, MD 20771, USA*

¹⁷*University of Massachusetts Amherst, 710 North Pleasant Street, Amherst, MA 01003-9305, USA*

¹⁸*Space Telescope Science Institute, Baltimore, MD, USA*

¹⁹*Department of Physics and Astronomy, Williams College, Williamstown, MA 01267, USA*

²⁰*Space Telescope Science Institute, Baltimore, MD, 21218, USA*

²¹*Laboratory for Multiwavelength Astrophysics, School of Physics and Astronomy, Rochester Institute of Technology, 84 Lomb Memorial Drive, Rochester, NY 14623, USA*

²²*Space Telescope Science Institute, 3700 San Martin Dr., Baltimore, MD 21218, USA*

²³*Gemini Observatory/NSF's National Optical-Infrared Astronomy Research Laboratory, 950 N. Cherry Ave., Tucson, AZ 85719, USA*

²⁴*Centro de Astrobiología (CAB), CSIC-INTA, Ctra. de Ajalvir km 4, Torrejón de Ardoz, E-28850, Madrid, Spain*

²⁵*U.S. Naval Observatory, 3450 Massachusetts Avenue NW, Washington, DC 20392, USA*

²⁶*Department of Physics and Astronomy, George Mason University, 4400 University Drive, MSN 3F3, Fairfax, VA 22030, USA*

²⁷*Department of Physics, 196 Auditorium Road, Unit 3046, University of Connecticut, Storrs, CT 06269*

ABSTRACT

We use *JWST*/NIRISS slitless spectroscopy from the Next Generation Deep Extragalactic Exploratory Public (NGDEEP) Survey to investigate the physical condition of star-forming galaxies at $1.7 < z < 3.4$. At these redshifts, the deep NGDEEP NIRISS slitless spectroscopy covers the [O II] $\lambda\lambda$ 3727,3729, [O II] $\lambda\lambda$ 4959,5007, H β and H α emission features for galaxies with stellar masses $\log(M_*/M_\odot) \gtrsim 7$, nearly a factor of a hundred lower than previous studies. We focus on the [O II]/[O III] (O₃₂) ratio which is primarily sensitive to the ionization state and with a secondary dependence on the gas-phase metallicity of the interstellar medium. We find significant ($\gtrsim 5\sigma$) correlations

Corresponding author: Lu Shen

lushen@tamu.edu

between the O_{32} ratio and galaxy properties as O_{32} increases with decreasing stellar mass, decreasing star formation rate (SFR), increasing specific SFR ($sSFR \equiv SFR/M_*$), and increasing equivalent width (EW) of $H\alpha$ and $H\beta$. These trends suggest a tight connection between the ionization parameter and these galaxy properties. Galaxies at $z \sim 2 - 3$ exhibit a higher O_{32} than local normal galaxies with the same stellar masses and SFRs, indicating that they have a higher ionization parameter and lower metallicity than local normal galaxies. In addition, we observe an evolutionary trend in the O_{32} – $EW(H\beta)$ relation from $z \sim 0$ and $z \gtrsim 5$, such that higher redshift galaxies have higher $EW(H\beta)$ and higher O_{32} at fixed EW. We argue that both the enhanced recent star formation activity and the higher star formation surface density may contribute to the increase in O_{32} and the ionization parameter.

Keywords: High-redshift galaxies(734); Star formation(1569); Galaxy stellar content(621); Galaxy evolution (594);

1. INTRODUCTION

Star formation is one of the fundamental processes that drive the evolution of galaxies and determine galaxies’ global properties. Globally, the cosmic star formation rate (SFR) density peaked between $z \sim 1$ and 3 (Madau & Dickinson 2014). Understanding the mechanisms behind star formation during this epoch and the factors leading to the subsequent decline is essential for a comprehensive picture of galaxy evolution. This requires investigating the physical conditions of star-forming regions within galaxies, particularly the ionized gas in the interstellar medium (ISM), where recently formed stars are embedded.

The physical properties of ISM are typically characterized by gas-phase metallicity and ionization parameters. The gas-phase metallicity has been extensively studied. The evolution of stellar mass and gas-phase metallicity relation has been characterized out to $z \sim 3$ with a clear trend of decreasing metallicity with redshift at fixed stellar mass (Erb et al. 2006; Maiolino et al. 2008; Cullen et al. 2014; Steidel et al. 2014; Sanders et al. 2018, 2021). In addition to a mass-metallicity relation, a secondary dependence of SFR has been observed (e.g., Ellison et al. 2008; Lara-López et al. 2010) and this mass-SFR-metallicity relation remains independent of redshift out to $z \sim 6$ (Mannucci et al. 2010; Zahid et al. 2014; Sanders et al. 2018; Topping et al. 2021; Curti et al. 2024). The interpretation of these relations and their evolution is that chemical enrichment depends on the galaxy’s star formation history and the interplay between gas infall and outflow.

In contrast, the evolutionary trends of ionization parameter have received little attention. The ionization parameter (q , or the dimensionless ionization parameter $U \equiv q/c$) is defined as the ratio between the mean hy-

drogen ionizing photon flux and the density of hydrogen atoms (Dopita & Sutherland 2003; Osterbrock & Ferland 2006). It is typically estimated from the ratio of emission lines of different ionization stages of the same element, such as the $[O\ III]/[O\ II]$ (O_{32}) ratio (e.g., Kewley & Dopita 2002; Kewley et al. 2019b). The correlation between the O_{32} ratio and the galaxy global properties such as stellar mass, SFR, and specific SFR ($sSFR \equiv SFR/M_*$) has been observed up to $z \sim 3$ (Nakajima & Ouchi 2014; Kewley et al. 2015; Sanders et al. 2016; Kaasinen et al. 2018; Mingozi et al. 2020; Papovich et al. 2022). These studies consistently found that star-forming galaxies (SFGs) at $z \sim 1 - 3$ have significantly higher O_{32} ratios than typical SFGs at $z \sim 0$ by ~ 0.6 dex at a fixed stellar mass. However, the physical cause of the elevated ionization parameter in high-redshift galaxies remains unclear.

It has been suggested that the evolution of the ionization parameter is correlated with the evolving equivalent width (EW) of H recombination lines and $sSFR$ (Kewley et al. 2015; Kaasinen et al. 2018). A high $sSFR$ (or EW) indicates a high ratio of young-to-old stars, which corresponds to a relatively increased flux of hydrogen-ionizing photons from young massive stars. Some other studies have pointed to the increased electron densities (n_e) in high redshift galaxies as a possible factor in increasing the ionization parameter (Davies et al. 2021; Reddy et al. 2023b,a). This is related to the fact that the ionization parameter is determined by hydrogen gas density, which is approximately the electron density (for an ionized gas). In addition, other factors such as low metallicity, a hard ionizing radiation field, and the presence of density-bounded H II regions could increase the O_{32} ratio (Nakajima & Ouchi 2014; Kewley et al. 2019b), which could bias the interpretation of O_{32} and the evolutionary trends of ionization parameter.

To gain a deeper understanding of the physical factors driving the elevated ionization parameter in high-

* NASA Postdoctoral Fellow

redshift galaxies, we investigate the ionization state of SFGs at $1.7 < z < 3.4$, using the deep, *JWST* NIRISS slitless spectroscopy observations from the Next Generation Deep Extragalactic Exploratory Public (NGDEEP) Survey (Bagley et al. 2022; Pirzkal et al. 2023; Shen et al. 2024). The NIRISS data probe observed-frame near-IR wavelengths ranging from 1.0-2.2 μm corresponding to rest-frame 0.37 - 0.81 μm and 0.23 - 0.50 μm for galaxies at $z = 1.7$ and $z = 3.4$, respectively. This data covers strong emission lines ([O II], H β , and [O III]) which trace gas ionization parameters and metallicities for galaxies at $z \sim 1.7 - 3.4$. Importantly, NGDEEP measures these properties for an unbiased galaxy sample with stellar masses of $\log(M_*/M_\odot) \gtrsim 7$ at these redshifts. This enables us to constrain the evolution of ISM properties (i.e., ionization and metallicity) and its correlation to galaxy properties in low-mass galaxies ($M_* < 10^9 M_\odot$). In this paper, we focus on the relationships between the O_{32} ratio and various galaxy properties, comparing them to those measured from local galaxies. We will present results on the evolution with metallicity in a future paper.

The outline for this paper is as follows. In Section 2 we describe the data sets, methods to derive stellar-population properties using broadband data, and sample selection. In Section 3, we present and constrain the relationships between the O_{32} ratio and galaxy properties, including stellar mass, SFR, sSFR, and EW of H α and H β . In Section 4, we discuss the dependence of the O_{32} ratio on the ionization parameter and metallicity, as well as the factors that could influence the ionization parameter. Finally, we summarize our findings in Section 5. Throughout this paper, all magnitudes are presented in the AB system (Oke & Gunn 1983; Fukugita et al. 1996). We adopt a standard Λ -cold dark matter (Λ CDM) cosmology with $H_0 = 70 \text{ km s}^{-1}$, $\Omega_{\Lambda,0} = 0.70$, and $\Omega_{M,0} = 0.30$ (Planck Collaboration et al. 2016).

2. DATA, METHOD, AND SAMPLE SELECTION

2.1. Optical/NIR Imaging and Photometry

We utilized a vast array of deep imaging taken with *HST* and *JWST* available in the HUDF field. This includes *HST* ACS F435W, F606W, F775W, F814W, and F850LP from the latest reductions processed as part of the Cosmic Assembly Near-IR Deep Extragalactic Legacy Survey (CANDELS, Koekemoer et al. 2011; Grogin et al. 2011). We include *JWST* NIR-Cam bands: F090W, F182M, F210M, F277W, F335M, F356W, F430M, F444W, F460M, and F480M from the JADES DR2 (Eisenstein et al. 2023; Rieke & the JADES Collaboration 2023; Williams et al. 2023). The *JWST* NIRISS direct-imaging from NGDEEP is not included

in the photometry catalog, because the same filters are covered by the NIRCam data, which are significantly deeper.

The photometry process is described in detail in Finkelstein et al. (2024). Here we summarize the salient steps. We matched the PSF of all ACS bands and all NIRCam bands bluer than F277W to that of the NIR-Cam F277W image. For bands redder than F277W, we calculated correction factors by convolving the F277W image to the larger PSF, and measuring the flux ratio in the native image to that in the convolved image. We performed photometry using SExtractor (Bertin & Arnouts 1996) in dual image mode, using the inverse-variance-weighted sum of the non-PSF-matched F277W and F356W images as the detection image. We ran the SExtractor in hot and cold modes (Finkelstein et al. *in prep.*). To combine these catalogs, we included all objects in the cold-mode catalog, and we included all objects in the hot-mode catalog whose central pixel did not lie in a cold-mode segmentation map, after that cold-mode segmentation map was dilated by a 5×5 kernel.

We measured flux densities for each galaxy in small Kron apertures. We apply two aperture corrections based on the ratio of the default Kron aperture to our small aperture and an additional aperture correction to measure flux missed on larger scales. We derived uncertainties on the flux densities by placing random non-overlapping apertures with diameters from 0.1-1.5'' in empty regions of the image. We fitted a four-parameter function to the normalized median absolute deviation (NMAD) in each aperture as a function of the aperture area. The flux uncertainty for each object is calculated from this fit for the area in a given object's aperture.

2.2. Grism Data Reduction and Line-flux Measurements

For the analysis of emission-line maps here, we processed the data using the GRIZLI version 1.9.5 (Brammer & Matharu 2021). GRIZLI performs full end-to-end processing of NIRISS imaging and slitless spectroscopic data sets, including retrieving, pre-processing the raw observations for cosmic rays, flat-fielding, sky subtraction, astrometric corrections, alignment, modeling contamination from overlapping spectra, extracting 1D and 2D spectra, and fitting full continuum+emission-line models. For this fitting process, GRIZLI uses a set of templates from the Flexible Stellar Populations Synthesis models (FSPS; Conroy & Gunn 2010) and nebular emission lines. The spectroscopic data is scaled to match the photometry catalog. GRIZLI determines a redshift by minimizing the χ^2 between observed 2D spectra and models. Then it fits emission-line fluxes using the

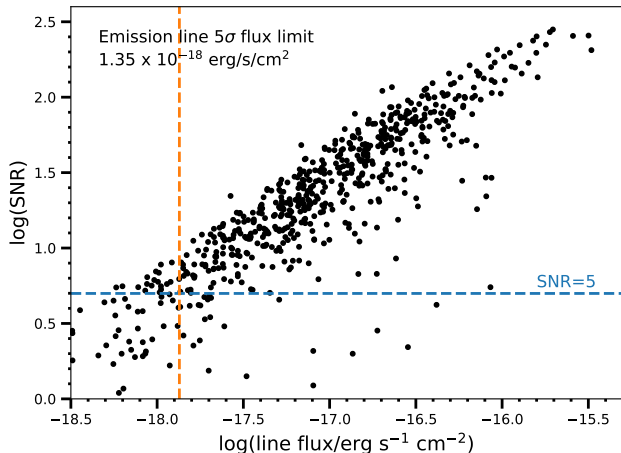


Figure 1. Signal-to-Noise Ratio (SNR) of emission lines as a function of emission line flux for NGDEEP galaxies at $1.7 < z < 3.4$. Emission lines include [O II] $\lambda\lambda$ 3727,3729, H β , [O III] $\lambda\lambda$ 4959,5007, and H α across three filters (F115W, F150W, and F200W).

best-fit redshift and accounts for the continua (correcting for absorption features, e.g., from Balmer lines) using the best-fit stellar population model. For additional details on GRIZLI and its data products, we refer the reader to Estrada-Carpenter et al. (2019); Simons et al. (2021); Matharu et al. (2021); Papovich et al. (2022); Wang et al. (2022); Simons et al. (2023); Noirot et al. (2023); Matharu et al. (2023).

We adopt the H α , H β , [O II], and [O III] emission line fluxes, equivalent widths, and associated errors measured by GRIZLI. For our selected NGDEEP sample (see Section 2.6), we measure the average emission line 5σ flux limit of 1.35×10^{-18} erg/s/cm 2 as shown in Figure 1. We note that due to the low spectral resolution of the NIRISS grism ($R \sim 150$), the H α and [N II] lines are blended. For the median stellar mass and redshift of the galaxies in our sample, we expect the [N II]/(H α + [N II]) to be ~ 0.05 (Faisst et al. 2018). It is worth noting that the flux measurement method employed by Pirzkal et al. (2023, and Vanderhoof in prep.) adopts more conservative flux uncertainties, which would imply the uncertainties on the line fluxes here are underestimated by a factor of ≈ 1.5 . We therefore adopt the flux uncertainties from GRIZLI for consistency, and we note that if we increased the errors by a factor of 1.5 it would not otherwise impact any of the findings in this paper.

2.3. SED Fitting and Estimating Galaxy Properties

We employed the SED fitting Code Investigating GALaxy Emission (CIGALE) (Boquien et al. 2019; Yang et al. 2020) to estimate properties of the stellar populations of our galaxies using the photometry catalog with

flux densities measured in bandpasses spanning the observed wavelength range of $0.43 - 4.8 \mu\text{m}$ (see details in Section 2.1). Note that the NIRISS spectra were not included in the fitting process. However, the redshift was fixed to the value determined from the NIRISS spectra as measured by GRIZLI (see Section 2.2).

Here we described the modules and parameters adopted in CIGALE. We adopted a delayed exponential star formation history (SFH) allowing the τ and stellar age to vary from 0.05–10 Gyr and 0.02–5 Gyr, respectively. In addition to the main star formation history, we allow for a more recent “burst” of star formation. We model this burst as an exponential SFH with a τ allowed to vary from 20 to 100 Myr with an age of 10 Myr and we allow the mass fraction of this burst (f_{burst}) to vary from 0 to 0.1. We assumed a Chabrier (2003) IMF and the stellar population synthesis models presented by Bruzual & Charlot (2003) with metallicity ranging from Solar (Z_{\odot}) to sub-Solar values ($0.4 Z_{\odot}$ and $0.2 Z_{\odot}$). We include nebular emission using templates of Inoue (2011). We allow the ionization parameter $\log(U)$ to vary between -3 to -1 , the gas metallicity (Z_{gas}) to vary between 0.002 and 0.02, and a fixed electron density of 100 cm^{-3} . The dust attenuation follows the extinction law of Calzetti et al. (2000) for attenuating the stellar continuum and it uses the Cardelli et al. (1989) extinction law with $R_V = 3.1$ for attenuating the emission lines. We allow the dust attenuation in emission lines from nebular regions $E(B-V)_{\text{gas}}$ to vary from 0 to 1.1, and a fixed dust attenuation ratio between emission lines and stellar continuum ($E(B-V)_{\text{star}}/E(B-V)_{\text{gas}} = 0.44$). The details of these parameters and values are listed in Table 1.

CIGALE calculates several different SFRs, including an instantaneous SFR ($\text{SFR}_{\text{instant}}$), and the SFR averaged over 10 Myr ($\text{SFR}_{10\text{Myrs}}$) and 100 Myr ($\text{SFR}_{100\text{Myrs}}$). These SFRs are influenced by the assumed parameterization and the fitted star formation history. To better understand these estimated SFRs, we compare the H α -derived and H β -derived SFRs with these SED-derived SFRs in Figure 2 for NGDEEP SFGs with H α and H β emission line flux Signal-to-Noise Ratios (SNRs) > 5 . The H α - and H β -derived SFRs are calculated from the dust-corrected H α /H β luminosity ratio using the Kennicutt & Evans (2012) calibration. We assume an intrinsic ratio of H α /H β = 2.86 (based on the Case B assumption for $T = 10^4$ K and $n_e = 10^2 \text{ cm}^{-3}$) when converting the H β luminosity to an SFR. See Section 2.4 for more details on the dust correction.

As shown in Figure 2, the instantaneous SFRs and $\text{SFR}_{10\text{Myrs}}$ from CIGALE correlate well with the SFRs derived from the H α and H β lines. The median dif-

ference between the SED-derived SFRs and the $H\alpha$ -derived SFRs are 0.08 and 0.07 dex, for the instantaneous and 10 Myr-averaged SFRs, respectively. However, the $SFR_{100\text{Myrs}}$ is on average lower than $H\alpha$ -derived SFR by 0.33 dex (a factor of order 2).

We adopt the Bayesian linear regression code LINMIX (Kelly 2007) to fit the relation between SED-derived and $H\alpha$ -derived SFRs, accounting for uncertainties on the two variables. The best-fit parameters are the median of the fitted parameters (the slope and intercept) from 10000 random draws from the posterior, and the associated errors are the average between the 16th and 84th percentiles of each parameter. This LINMIX method is applied throughout the paper to derive fit lines. The best-fitted lines for SFR_{instant} and $SFR_{10\text{Myrs}}$ align well with the 1-to-1 relation. The 1σ dispersion values are similar (~ 0.2 dex) in both cases. In contrast, the best-fitted line for $SFR_{100\text{Myrs}}$ is offset from the 1-to-1 relation by ~ 0.3 dex and has a slightly larger scatter (0.25 dex). This is consistent with the fact that the $H\alpha$ emission is sensitive to ionization from O-type stars with lifetimes of ~ 5 Myr. In addition, we found similar trends when comparing SED-derived SFRs and $H\beta$ -derived SFRs with slightly larger differences of 0.19, 0.23, and 0.45 dex for SFR_{instant} , $SFR_{10\text{Myrs}}$, and $SFR_{100\text{Myrs}}$, respectively. Thus, we adopt the SFR averaged over 10 Myr as the SED-derived SFR and their associated errors. In addition, we adopt the stellar mass (M_*) and the color excess of the stellar continuum $E(B-V)_{\text{star}}$ from CIGALE SED fitting. The sSFR is calculated as $\text{sSFR} \equiv SFR_{10\text{Myr}}/M_*$.

2.4. Dust reddening correction

Ideally, we would use the Balmer decrements (e.g., measured from the $H\alpha/H\beta$ line ratios) to estimate nebular dust attenuation. However, because not all galaxies have both $H\beta$ and $H\alpha$ covered by NIRISS, we instead rely on the $E(B-V)$ values derived from SED fitting. To confirm the reliability of the $E(B-V)$ from SED fitting, we compared them with the $E(B-V)_{\text{gas}}$ calculated from the $H\alpha/H\beta$ line ratios for NGDEEP SFGs that have both $H\alpha$ and $H\beta$ emission line fluxes with $\text{SNR} > 5$. In the top panel of Figure 3, we show the histogram of the $H\alpha/H\beta$ line ratios. There are 50% of the 69 galaxies having $H\alpha/H\beta$ ratios lower than the Case B value of 2.86. This is also found in Pirzkal et al. (2023) which used NGDEEP epoch 1 data and adopted a different data reduction and extraction method. We apply a Gaussian fitting to the $H\alpha/H\beta$ -derived $E(B-V)_{\text{gas}}$ after performing 3σ clipping. The best-fit Gaussian fit has a mean of -0.02 and a standard deviation of 0.27.

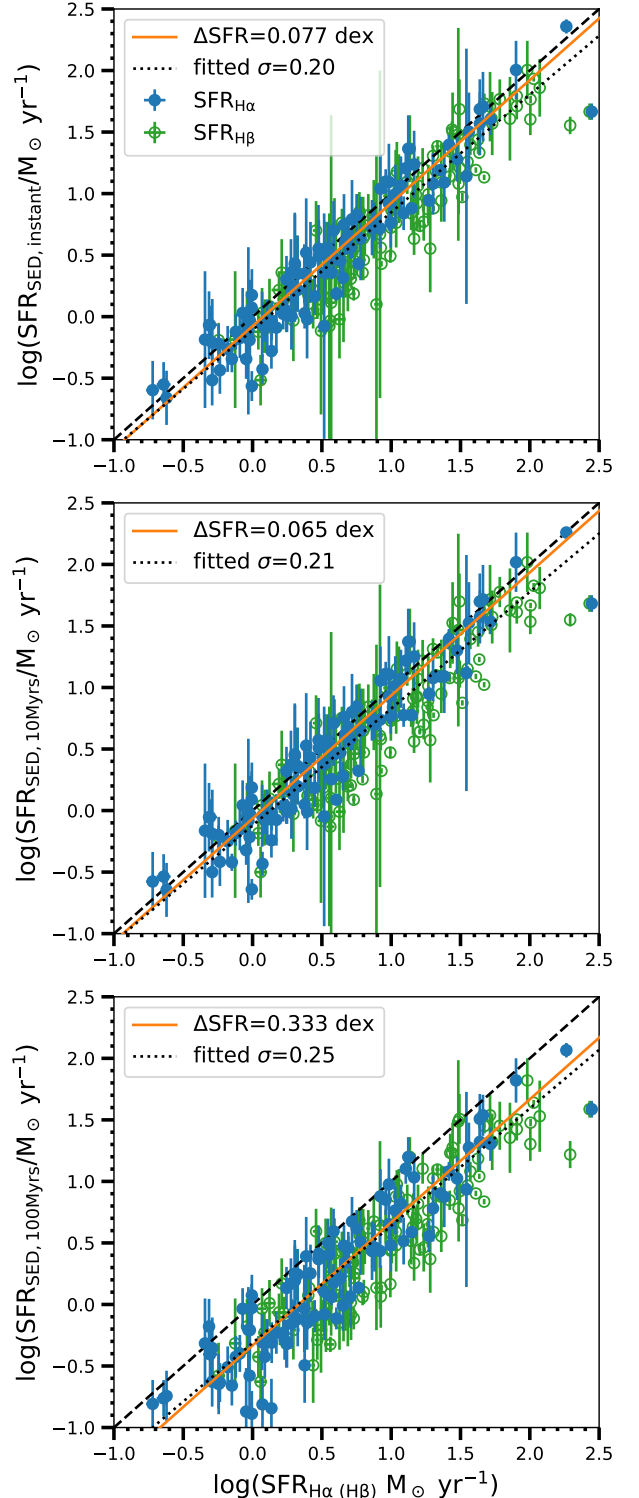


Figure 2. Comparison of the SED-derived instantaneous SFR (*top*), and the SFR averaged over 10 Myr (*middle*) and average over 100 Myr (*bottom*) and $H\alpha$ - and $H\beta$ -derived SFR for NGDEEP full sample with $H\alpha$ and $H\beta$ $\text{SNR} > 5$, respectively. In each panel, the solid orange line shows the median difference between the SFR_{SED} and $SFR_{H\alpha}$. The dotted black line shows the best-fitted line using LINMIX package (Kelly 2007) with the 1σ dispersion values marked. The black dashed line is the 1-to-1 relation.

Table 1. Parameters used in the SED fitting with CIGALE.

Parameter	Values
Star formation history (sfhdelayed)	
τ [Myr]	50, 100, 300, 500, 1000, 2000, 3000, 5000, 10000
Age [Myr]	20, 40, 80, 160, 320, 640, 1280, 2000, 3000, 5000
τ_{burst}	20, 50, 100
age_{burst}	10
f_{burst}	0.0, 0.01, 0.05, 0.1
Simple stellar population (Bruzual & Charlot 2003)	
IMF	Chabrier (2003)
Metallicity Z_*	0.004, 0.008, 0.02
Nebular emission (Inoue 2011)	
$\log(U)$	-3, -2.5, -2.0, -1.5, -1
gas metallicity Z_{gas}	0.002, 0.005, 0.011, 0.02
Dust Attenuation (Calzetti et al. 2000)	
$E(B-V)_t$	0, 0.01, 0.05, 0.1, 0.15, 0.2, 0.3, 0.5, 0.7, 0.9, 1.1
$E(B-V)_{factor}$	0.44

The mean value being close to zero indicates the negative $E(B - V)_{gas}$ values are more likely due to measurement uncertainties. Meanwhile, this standard deviation represents the total uncertainties on the $E(B - V)$.

We compared the SED-derived $E(B - V)_{star}$ and $H\alpha/H\beta$ -derived $E(B - V)_{gas}$ and shown in the bottom panel of Figure 3. For those with $H\alpha/H\beta > 2.86$, the SED-derived $E(B - V)_{star}$ and $H\alpha/H\beta$ -derived $E(B - V)_{gas}$ generally follow the $E(B - V)_{star} = 0.44 \times E(B - V)_{gas}$. We measure a median star-to-gas attenuation ratio of 0.56. For those with $H\alpha/H\beta < 2.86$, they tend to have low SED-derived $E(B - V)_{star}$ with the median $E(B - V)_{star}$ of 0.11, suggesting that the dust attenuation is relatively low in these galaxies.

Therefore, in this paper, for the dust correction of emission lines (i.e., [O III] $H\beta$, [O II] $H\alpha$), we adopt the $E(B - V)_{star}$ from the SED fits, convert to the $E(B - V)_{gas}$ for nebular emission line by dividing 0.44, and follow the Cardelli et al. (1989) extinction model with $R_V = 3.1$. For the dust correction of the continuum, we adopt the $E(B - V)_{star}$ from the SED fits and follow the Calzetti et al. (2000) extinction model with $R_V = 3.1$. These extinction laws and factors are consistent with those adopted during the SED fitting (see Section 2.3).

After applying the dust correction, the O_{32} ratios decrease on average by 0.15 dex. The impact of dust cor-

rection increases as the O_{32} ratio, with a scatter ranging from 0.08 to 0.26 dex from the 16th/84th percentile. We note that the results of this paper remain unchanged if we assume no dust for galaxies with $H\alpha/H\beta < 2.86$ or if we adopt a slightly higher star-to-gas attenuation ratio of 0.56.

2.5. The [O III]/[O II] ratio

Here we focus on the relation between the [O III]/[O II] line ratio and galaxy properties (i.e., stellar mass and star formation). The [O III]/[O II] ratio measures the relative amount of emission from double-ionized oxygen to singly ionized oxygen, which traces the ionization of the gas (e.g., Kewley et al. 2019b). We defined the line ratio O_{32} as:

$$O_{32} \equiv \frac{[\text{O III}] \lambda\lambda 4959, 5008}{[\text{O II}] \lambda\lambda 3727, 3729} \quad (1)$$

where [O III] $\lambda\lambda 4959, 5008$ and [O II] $\lambda\lambda 3727, 3729$ are the sum of the emission from both lines in the doublets (as these are unresolved in the NIRISS spectra) and dust corrected as described in section 2.4. For those with [O II] SNR < 5 , we use the $5 \times$ [O II] flux error as an upper limit on [O II] and, thus, a lower limit on the O_{32} ratio. The uncertainties in O_{32} ratio include the uncertainties on emission lines and $E(B - V)_{star}$.

2.6. Sample Selection

Here we use the NGDEEP NIRISS WFSS spectroscopy to study galaxies with [O II] $\lambda\lambda 3727, 3729$ and [O III] $\lambda\lambda 4959, 5008$, with the ratio of these two emission lines tracing the ionization parameter. Our NIRISS F115W+F150W+F200W data cover both lines for galaxies in the redshift range $1.72 < z < 3.44$. Additionally, the data include coverage of $H\beta$ $\lambda 4862$ for all galaxies. For galaxies at $1.72 < z < 2.22$, the data also include coverage of $H\alpha$ $\lambda 6564$ + [N II] $\lambda 6548, 6584$.

We selected galaxies from NGDEEP for this study using the following criteria and summarized in Table 2

1. We visually examined all the GRIZLI extractions with F150W AB magnitude < 28.4 , requiring galaxies to have at least one spectral feature detected (i.e., emission line, absorption feature, and D4000 break) and to be well-fitted with GRIZLI. The F150W magnitude cut was chosen because the fraction of galaxies with “good” spectra is very low ($< 1\%$) at magnitudes fainter than 28.4. Visual examination ensures that the derived redshifts are reliable and that the spectra are not affected by contamination from nearby objects. We identified 498 galaxies through this process.

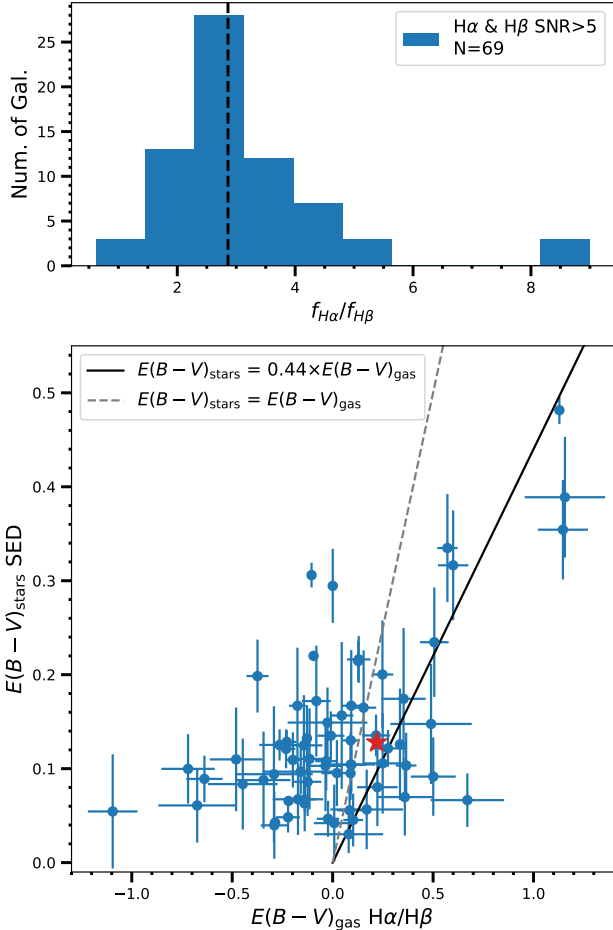


Figure 3. *Top:* Histogram of $H\alpha/H\beta$ emission line ratios for NGDEEP final sample with $H\alpha$ and $H\beta$ SNR > 5 . The vertical dashed line marks the theoretical minimum value of 2.86 in the absence of dust for Case B recombination. *Bottom:* Comparison of the color excesses derived for the stellar continuum from SED fitting and that for the ionized gas calculated from $H\alpha/H\beta$. The $E(B-V)_{\text{gas}}$ is computed assuming the Cardelli et al. (1989) extinction curve with $R_V = 3.1$. The median stellar-to-gas attenuation ratio for galaxies with $H\alpha/H\beta > 2.86$ is marked by a red star. The black solid line shows the relation $E(B-V)_{\text{star}} = 0.44 \times E(B-V)_{\text{gas}}$ from Calzetti et al. (2000). The grey dashed line shows the 1-to-1 relation between $E(B-V)_{\text{star}}$ and $E(B-V)_{\text{gas}}$.

2. We required the spectroscopic redshift derived from the NIRISS data to lie in the redshift range of $1.72 < z < 3.44$. This redshift range ensures that [O II] and [O III] are mostly covered by grism. A total of 243 galaxies were identified at this stage. Because the NIRISS grism filters do not overlap in the wavelength, galaxies with [O II] or [O III] near the edges of the filters were further excluded in step 5.

3. We rejected galaxies identified as AGN by cross-matching to the latest AGN catalog from Lyu et al. (2022) within $1''$. This step removed 9 galaxies identified as AGN.
4. We selected SFGs and quiescent galaxies following the UVJ color-color selection criteria from Whitaker et al. (2011). Four quiescent galaxies are removed in this step.
5. We performed a second, more detailed quality check of the GRIZLI extractions. In this step, we identified and masked contamination if it affects the emission line region of a galaxy. We then re-ran the GRIZLI fitting, excluding the masked regions. During this step, we also removed any objects where their [O II] or [O III] emission fell too close to the edge of the NIRISS wavelength range, or if GRIZLI failed to remove contamination, or the redshift changed after contamination was removed. We obtained a total of 177 galaxies following this step. We denote this as the “full sample” and is the main sample in this paper. All of these galaxies have [O III] detections at $> 5\sigma$ in the combined 1D spectra, because the [O III] is the strongest line for the majority of these galaxies, and the redshift identification mostly relies on this emission line. This does open a selection bias (as we require strong lines for selection), and we will further discuss this effect in Section 4.1.

6. Lastly, we require the detection of both [O II] and [O III] emission lines with SNR > 5 in the combined 1D spectra. This produced a sample of 148 galaxies, which we denote as the “final sample”. We also consider and plot those with [O II] SNR < 5 (which we call the “low-SNR sample”), but these galaxies are not included in the calculation of median values or linear relations. Within the final sample, 119 and 78 galaxies have $H\beta$ and $H\alpha$ SNR > 5 , respectively. These samples will be used in Section 3.5.

In the top panel of Figure 4, we show the stellar mass histograms for the full sample, the final sample, and for all “photometric” galaxies in the dataset (including those with photometric redshifts, or spectroscopic redshift if available) in the range of $1.7 < z < 3.4$. The histogram for the photometric galaxy sample is rescaled to match the massive end of that for NGDEEP galaxies. The stellar mass histogram of the full and final samples diverges from that for the photometric galaxies at $\lesssim 10^{8.5} M_{\odot}$.

Table 2. Summary of Sample Selection

Sample Selection Criteria	Galaxies
F150W magnitude < 28.4 and quality check	498
Spec-z at $1.72 < z < 3.44$	243
AGN removed	234
SFGs with UVJ color selection	230
full sample: Quality check & refit	177
final sample: [O III] & [O II] SNR>5	148
low-SNR sample:	29
[O III] SNR > 5 & [O II] SNR<5	
final sample with $H\beta$ SNR>5	119
final sample with $H\alpha$ SNR>5	78

NOTE—The names of the samples used throughout this paper are denoted in bold.

The final sample has a similar histogram as the full sample at the massive end, with a small difference present at lower mass.

The bottom panel of Figure 4 shows a probability density function (PDF) of stellar mass for the NGDEEP full sample and also with the galaxies separated by redshift with $1.7 < z < 2.5$ and $2.5 < z < 3.4$. The median stellar mass are $10^{8.51} M_{\odot}$ and $10^{8.40} M_{\odot}$ for $z \sim 2$ and $z \sim 3$, respectively. We adopt the peak of stellar mass PDF as the 50% mass completeness by fitting a skew-normal distribution with scipy skewnorm package. The 50% mass completeness is $10^{8.40} M_{\odot}$ for galaxies in the full sample, which is the same when separated in redshift. Throughout the paper, we therefore adopt $10^{8.40} M_{\odot}$ as our mass completeness. In particular, we will show all galaxies in our samples in subsequent figures, but we only use galaxies with stellar mass above this limit for fitting linear relations.

2.7. Comparison Galaxy Samples

For comparison, we consider both the nearby samples and galaxies at similar redshifts from the literature. For $z \sim 1 - 2$, we consider two samples: the CANDELS Ly α Emission At Reionization (CLEAR) survey, which measured [O II], [O III], and $H\beta$ emission features for 196 galaxies at $z \sim 1.1 - 2.3$ using HST WFC3 grisms (Pavovich et al. 2022); the MOSFIRE Deep Evolution Field (MOSDEF) survey, which obtained spectra for ~ 400 galaxies at $z \sim 0.8 - 4.4$ using Keck/MOSFIRE (Kriek et al. 2015; Reddy et al. 2015). From CLEAR, we selected 158 galaxies with SNR > 3 for both [O II] and [O III] emission lines. The dust correction is calculated following the (Calzetti et al. 2000) extinction curve and

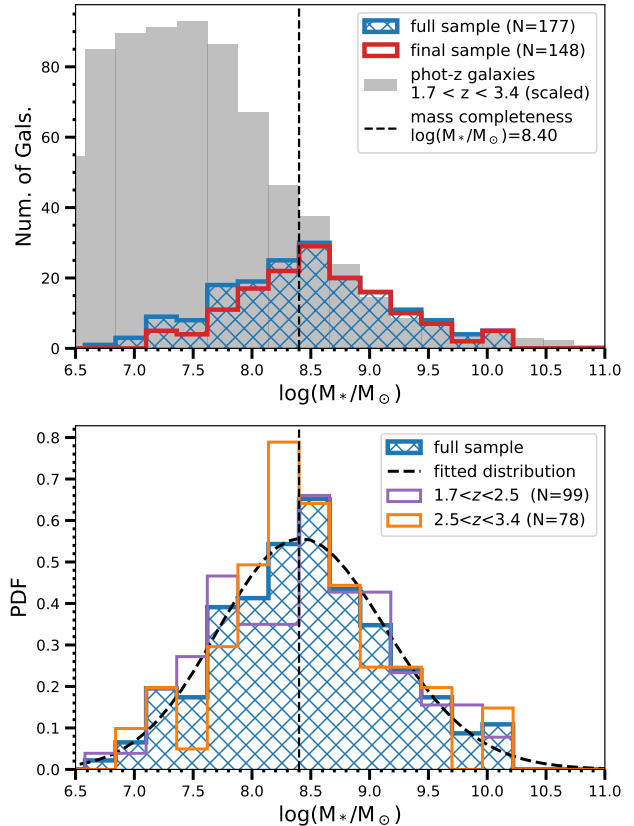


Figure 4. *Top:* The stellar mass histograms for NGDEEP full sample (blue), final sample (red), and “photometric” galaxies. The latter includes all galaxies with photometric redshift (spectroscopic redshift if available) at $1.7 < z < 3.4$ (grey). The histogram for the photometric galaxies is rescaled to match the massive end of that for NGDEEP galaxies. *Bottom:* The probability density function (PDF) of stellar mass for NGDEEP full sample (blue), and the full sample separated by redshift with $1.7 < z < 2.5$ and $2.5 < z < 3.4$ (purple and orange, respectively). The fitted skew normal distribution for NGDEEP galaxies is shown in a black dashed line. In both panels, the vertical dashed line marks the mass completeness of $10^{8.40} M_{\odot}$.

using the A_V from SED fitting. Stellar mass and SFR are estimated using the SED fitting assuming a Kroupa (2001) IMF. From MOSDEF, we selected 75 galaxies with SNR > 3 for all [O II], $H\beta$, [O III] and $H\alpha$ emission lines. The [O II] flux is obtained by adding [O II] $\lambda 3726$ and [O II] $\lambda 3729$ fluxes and the [O III] flux is obtained by multiplying the [O III] $\lambda 5007$ flux by $(1+1/2.98)$, which is the ratio of [O III] $\lambda 4959$ to [O III] $\lambda 5007$ fluxes. The dust correction is estimated using $H\alpha/H\beta$ assuming an intrinsic ratio of 2.86 and following the (Cardelli et al. 1989) extinction curve. We adopt the stellar mass from the 3D-HST catalog from Skelton et al. (2014) and the SFR

measured by adding the rest-frame UV and re-radiated IR light from Whitaker et al. (2014).

For $z \sim 0$, we consider four samples: the Sloan Digital Sky Survey (SDSS); the Cosmic Origins Spectrograph Legacy Spectroscopic Survey (CLASSY) treasury (Berg et al. 2022); green pea galaxies (Yang et al. 2017b); and blueberry galaxies (Yang et al. 2017a). The latter two samples are named for their compact and distinctive green and blue colors in SDSS false-color *gri*-band images. The SDSS sample represents the overall $z \sim 0$ population, while the latter three samples are selected to be UV bright (CLASSY) or to have strong emission lines (green peas and blueberry galaxies), which may have properties more similar to those of high redshift galaxies. For the SDSS sample, we adopt emission-line measurements and galaxy properties from the MPA-JHU catalog of measurements for SDSS DR8 (Brinchmann et al. 2004; Kauffmann et al. 2003; Tremonti et al. 2004). We select galaxies with $\text{SNR} > 3$ in all [O II], H β , [O III], and H α emission lines, and selected SFGs based on a BPT diagram (Baldwin et al. 1981). Again, to compare these results to those of our NGDEEP samples, the [O II] flux is obtained by adding [O II] λ 3726 and [O II] λ 3729 fluxes, and the [O III] flux is obtained by multiplying [O III] λ 5007 flux with $(1+1/2.98)$. The dust correction is calculated with H α /H β assuming an intrinsic ratio of 2.86 and following the (Cardelli et al. 1989) extinction curve. We adopted the median estimate of the total stellar mass and SFR PDF as the final stellar mass and SFR. Note that SFRs are derived by combining emission-line measurements and correcting for aperture loss.

For the CLASSY sample, we adopt measurements for all 45 galaxies from (Berg et al. 2022). The O_{32} ratio of CLASSY sample is measured with [O III] λ 5007/[O II] λ 3726,3729. To match our O_{32} ratio, we multiply the CLASSY O_{32} ratio by $(1+1/2.98)$. For green pea galaxies, we adopted all 43 galaxies with all [O II], H β , [O III], and H α $\text{SNR} > 3$. For blueberry galaxies, we adopted all 36 galaxies with all [O II], H β , and [O III] $\text{SNR} > 3$. No dust correction is applied for blueberry galaxies because the H α fluxes were probably underestimated due to the poor calibration in the red end of spectra (see more in Yang et al. 2017a). SFR is calculated from H β for blueberry galaxies and dust-corrected H α for green pea galaxies using the Kennicutt & Evans (2012) calibration.

The SDSS, CLASSY, green pea, and blueberry galaxy catalogs all have [O II] and [O III] measurements, allowing us to compare O_{32} and galaxy properties across samples. However, we note that galaxies' properties are derived using different SED fitting methods with different wavelength coverage of photometry, which could result

in biases during the comparison to our work. In the case of the SFR, our SED-derived SFR values are consistent with H α -derived SFR, where the latter is used to derive SFRs for the SDSS, green pea, and blueberry galaxies. We also find a consistent H α -derived SFR and the adopted UV+IR SFR for the MOSDEF galaxies, with an average difference of -0.07 dex. In terms of stellar mass, it is less sensitive to the adopted method and photometry data coverage. In addition, most of these comparison catalogs assumed the same Chabrier (2003) IMF and only CLEAR assumed a Kroupa (2001) IMF. We expect this difference in IMF to have a negligible impact on the derived galaxy properties.

3. RESULTS

3.1. The SFR – Stellar Mass Relationship

The left panel of Figure 5 shows the SED-derived SFRs and stellar masses for galaxies in the NGDEEP final sample and low-SNR sample. The figure also shows the median SFRs and stellar masses of galaxies in the final sample divided into redshift bins of $1.7 < z < 2.5$ and $2.5 \leq z < 3.4$. The median and associated uncertainties are calculated with a bootstrap method to account for uncertainties on individual measurements and the scatter in each bin following Shen et al. (2023). The binning is chosen to have a similar number of galaxies in each bin, with a minimum of 10 galaxies per bin.

We color-code individual galaxies by redshift in the left panel of Figure 5. There is a clear trend with redshift such that SFGs have higher SFR with increasing redshift at fixed stellar mass. This is consistent with the redshift evolution of the SFR- M_* relation found by previous studies (e.g., Whitaker et al. 2014; Tomczak et al. 2016).

For comparison, we show the star-formation main-sequence (SFMS) derived from a larger sample of SFGs selected from the UVJ color-color method at $2.0 < z < 2.5$ from Whitaker et al. (2014). We compare our galaxies with this SFMS using galaxies having stellar mass above the mass completeness limits of the Whitaker et al. (2014) samples ($\sim 10^{9.2} M_\odot$). Our galaxies have a higher SFR than the Whitaker et al. (2014) SFMS with a median difference of $\log(\text{SFR}/\text{SFR}_{\text{MS}}) = 0.36$ dex and a scatter from -0.01 to 0.65 dex from the 16th/84th percentile. This bias is similar to other studies of emission-line selected studies of galaxies (Sanders et al. 2016; Papovich et al. 2022), such that emission-line samples of SFGs tend to have higher SFRs at fixed stellar mass. We will discuss this effect in our results in Section 4.1.

In addition, we find that the median SFR values of galaxies with $M_* < 10^8 M_\odot$ at $z < 2.5$ do not decrease with decreasing stellar mass. Instead, galaxies in the

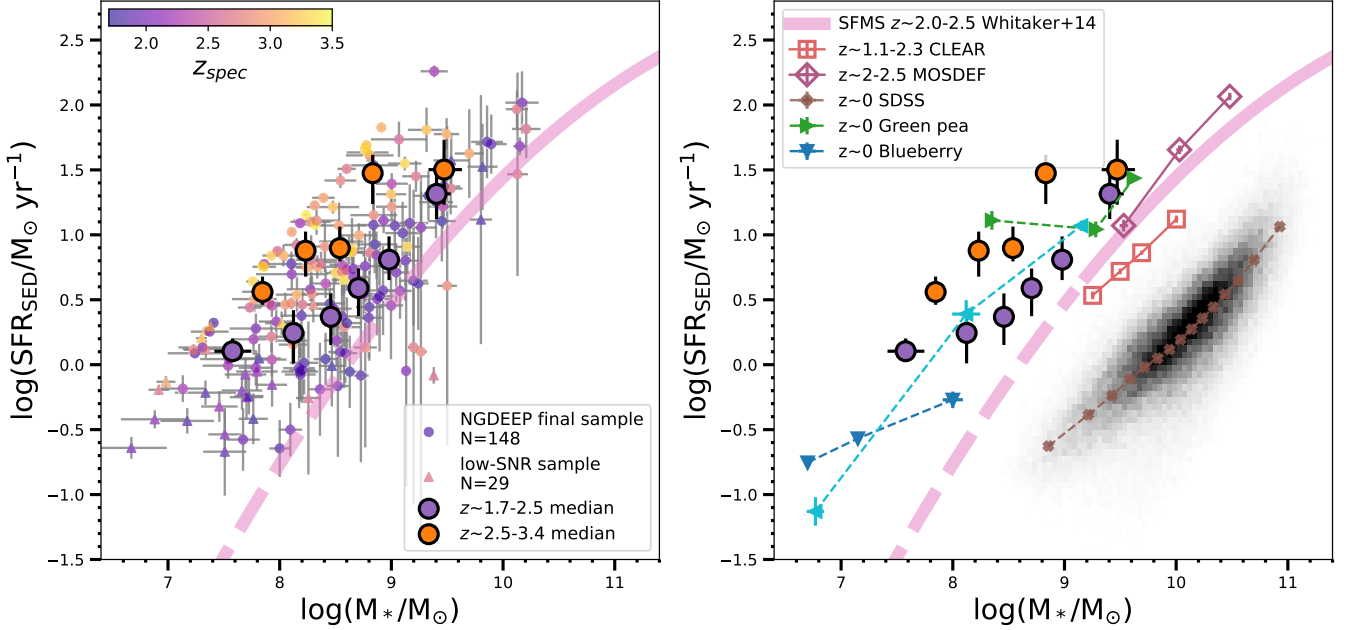


Figure 5. *Left:* The SED-derived SFR versus the stellar mass for galaxies in the NGDEEP final sample (dots) and low-SNR sample (triangle) color-coded by their redshift. The median SFR and stellar mass for galaxies in the final sample at $z \sim 1.8 - 2.5$ and $z \sim 2.5 - 3.4$ are shown (in both panels) in black purple- and orange-filled dots, respectively. For comparison, the SFMS for galaxies at $2.0 < z < 2.5$ from Whitaker et al. (2014) is shown down to their mass completeness in the pink line and extended to the lower stellar mass region in the dashed line. *Right:* The median SFR and stellar mass for galaxies at $z \sim 1 - 2$ from CLEAR (Papovich et al. 2022, open orange squares) and at $z \sim 2 - 2.5$ from MOSDEF (Sanders et al. 2016, open magenta diamonds), $z \sim 0$ SDSS galaxies (brown crosses), CLASSY galaxies (Berg et al. 2022, cyan triangles), green pea galaxies (Yang et al. 2017b, green triangles) and blueberry galaxies (Yang et al. 2017a, blue triangles). The SDSS sample is shown in the 2D histograms in black. The same median values from the NGDEEP final sample as *left* are shown in black purple- and orange-filled dots. The NGDEEP O_{32} sample has consistently higher SFR than the SFMS at $z \sim 2 - 2.5$, and has a similar SFR with those of extreme local galaxies at $z \sim 0$.

low-SNR sample dominate in this low-mass, low-SFR region. Therefore, the flattened median at low mass is mostly likely due to the detection limit, where galaxies with lower SFR have [O II] (or even [O III]) emission below the detection limit.

The median stellar mass and SFR of local and $z \sim 1 - 2$ samples are shown in the right panel of Figure 5. The uncertainties on the median are given by $\sigma_{\text{MAD}}/\sqrt{n-1}$, where σ_{MAD} is the median absolute deviation and n is the number of the galaxies in each bin. The CLEAR sample from *HST* grism observations is on average more massive ($10^{9.2} - 10^{10} M_{\odot}$) and has lower SFR values than the NGDEEP final sample, due to the lower redshifts of the CLEAR galaxies. The MOSDEF galaxies are also more massive, spanning stellar mass between $10^{9.5} - 10^{10.5} M_{\odot}$. They generally follow the SFMS at $z \sim 2.0 - 2.5$. The SFR- M_* of the extreme local galaxies from the CLASSY, “blueberries”, and “green pea” samples is consistent with that of the NGDEEP final sample, suggesting the properties and physical conditions of these galaxies are comparable with our $z \sim 2 - 3$

galaxies. On the other hand, the SDSS sample has significantly lower SFR at the same stellar mass compared to galaxies at intermediate redshift and those extreme local galaxies.

3.2. The Mass - O_{32} Relation

Figure 6 shows a tight relationship between the O_{32} ratio and the stellar mass of our final sample, such that the O_{32} ratio decreases as stellar mass increases. We adopt a Spearman rank correlation test to assess the correlation between stellar mass and O_{32} ratio. The test returns a correlation coefficient of -0.78 and a p-value¹ of $\sim 10^{-32}$. This test confirms the significant correlation between O_{32} and stellar mass. The correlation remains significant when separating in redshift.

¹ The p-value quantifies the probability of obtaining the observed data assuming the null hypothesis (i.e., no correlation) is true. The significance of the correlation by giving the probability that the data are uncorrelated (i.e., the null hypothesis). We reject the null hypothesis if the p-value is ≤ 0.05 , which suggests that the observed correlation is statistically significant.

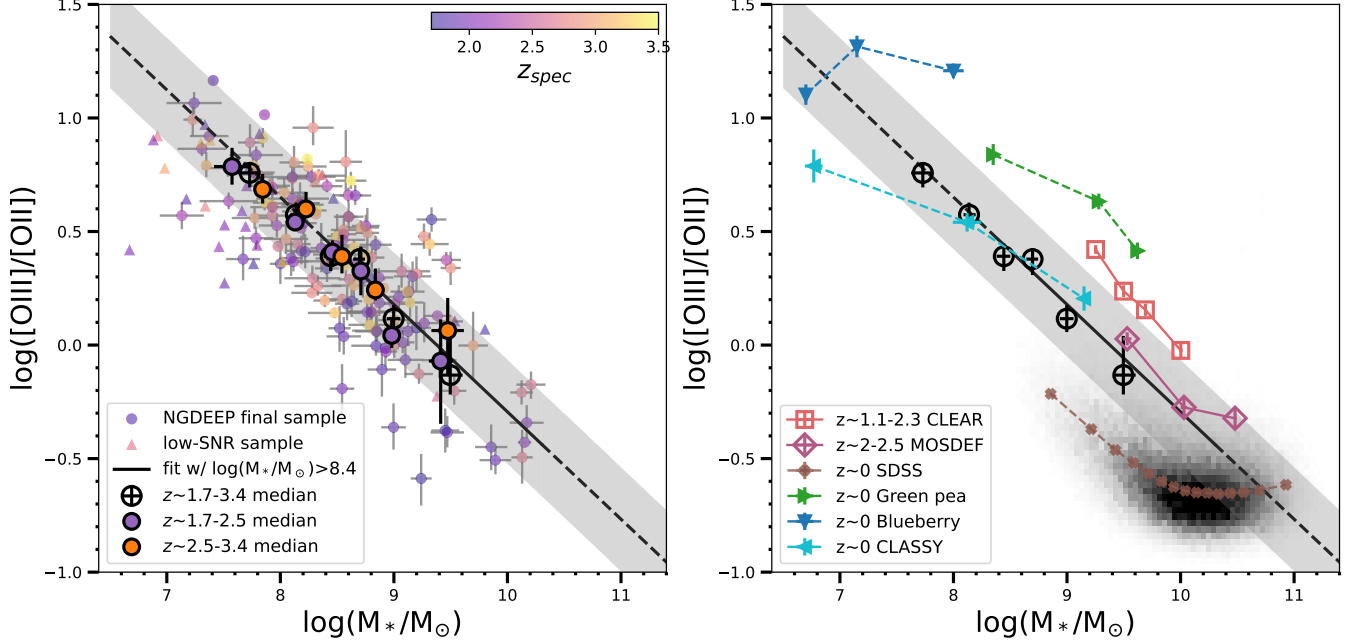


Figure 6. *Left:* The O_{32} ratio versus stellar mass for galaxies in the NGDEEP final sample (dots) and low-SNR sample (triangle), color-coded by redshift. The median O_{32} along the abscissa are shown for galaxies in the final sample (open black circles), for those at $1.7 < z < 2.5$ and at $2.5 \leq z < 3.4$ in purple- and orange-filled dots, respectively. The best fit for the NGDEEP final sample with stellar mass $> 10^{8.4} M_{\odot}$ is shown as the solid black lines, and extended to lower stellar mass as the dashed line. The grey region marks the 1σ total scatter. *Right:* The median O_{32} ratios as a function of stellar mass for CLEAR galaxies at $z \sim 1 - 2$ (open orange squares), MOSDEF galaxies at $z \sim 2 - 2.5$ (open magenta diamonds), $z \sim 0$ SDSS galaxies (brown crosses), CLASSY galaxies at $z \sim 0$ (cyan triangles), green pea galaxies at $z \sim 0$ (green triangles) and blueberry galaxies at $z \sim 0$ (blue triangles). The SDSS sample is shown in the 2D histograms in black. The same median values and fits from the NGDEEP final sample are shown, identical to those in the *left* panel. The NGDEEP sample shows a tight mass- O_{32} relation without redshift evolution between $z \sim 1.7 - 3.4$.

We color-coded galaxies in the full sample by redshift in the left panel of Figure 6. We measure the median O_{32} in stellar mass bins for galaxies in the final sample and those in two redshift bins of $1.7 < z < 2.5$ and $2.5 \leq z < 3.4$. We do not find any clear evidence of a redshift dependence on the mass- O_{32} relation.

We adopt the LINMIX to quantify the mass- O_{32} relation using galaxies in the final sample with stellar mass above the mass completeness limit ($> 10^{8.4} M_{\odot}$). As a result, we find

$$\log(O_{32}) = (4.44 \pm 0.53) + (-0.47 \pm 0.06) \times \log(M_{*}), \quad (2)$$

where M_{*} has units of M_{\odot} , and where the median intrinsic scatter measured by LINMIX is 0.04 dex. The total scatter of the mass- O_{32} relation is 0.23 dex. We show the fit extrapolated to lower stellar mass in Figure 6. The median values follow the fitted line to the lowest stellar mass bin $\sim 10^{7.5} M_{\odot}$.

We obtain similar slopes and intercepts when fit to galaxies at $1.7 < z < 2.5$ and $2.5 \leq z < 3.4$, with slopes of -0.53 ± 0.09 and -0.42 ± 0.08 , and intercepts of 4.92 ± 0.79 and 3.98 ± 0.68 , respectively. These fit

results, along with the consistent median values, suggest no significant redshift evolution of the mass- O_{32} relation between $z \sim 1.7 - 3.4$.

In comparison, we show the distribution of O_{32} and stellar mass for the local and $z \sim 1 - 2$ samples in the right panel of Figure 6. Galaxies from MOSDEF are generally consistent with the fitted mass- O_{32} relation, with an average slightly higher O_{32} at fixed stellar mass by 0.12 dex. CLEAR galaxies are on average higher than the mass- O_{32} relation by a median of 0.28 dex. The CLEAR sample has on average lower SFR than NGDEEP and MOSDEF as shown in Figure 5. As shown in Section 3.3 (and Figure 7), we find an anti-correlation between O_{32} and SFR, which could explain the higher O_{32} for CLEAR sample. The median trend of MOSDEF galaxies appears to flatten at high stellar masses $\sim 10^{10} M_{\odot}$, consistent with the median trend observed in SDSS galaxies (also see Sanders et al. 2016). We do not see this flattening in our sample, likely because our sample consists mainly of galaxies in the stellar mass range of $10^8 - 10^{9.2} M_{\odot}$ (16th to 84th percentile), and lacks more massive galaxies.

The mass- O_{32} relation clearly evolved from $z \sim 0$ from SDSS to $z \sim 2$ from NGDEEP, CLEAR, and MOSDEF. The median O_{32} versus M_* values for SDSS show an anti-correlation at low mass ($\sim 10^9 - 10^{10} M_\odot$) and flattened at high stellar mass. At fixed stellar mass, galaxies have a higher O_{32} at a higher redshift, and the effect is stronger for galaxies of lower stellar mass. The difference of O_{32} is 0.46 dex at $M_* \sim 10^9 M_\odot$. These results suggest that galaxies at $z \sim 1 - 3$ generally have higher ionization parameters compared to local galaxies at the same stellar mass, assuming the same relation between O_{32} and ionization parameters at both redshifts.

We then compare to those extreme galaxies at $z \sim 0$. The median O_{32} ratios of CLASSY galaxies align with our mass- O_{32} relation at stellar mass $\gtrsim 10^8 M_\odot$. This consistency indicates that these galaxies have similar ISM physical conditions as galaxies at $z \sim 2.5$. At low stellar mass $< 10^8 M_\odot$, the median O_{32} ratio of CLASSY galaxies shows lower O_{32} than our extrapolated line. Due to the limited number of galaxies at these lower stellar masses, we cannot draw any definitive conclusions. Green peas have higher O_{32} than our $z \sim 2.5$ relation at the same stellar mass, suggesting that these galaxies have higher ionization parameters and/or lower metallicity than $z \sim 2.5$ galaxies. Blueberry galaxies have similar to higher O_{32} compared to the extended $z \sim 2.5$ relation, but they extend to lower stellar mass regions. Also note that no dust correction is applied for blueberry galaxies, which would slightly lower the O_{32} though the correction is expected to be minor for galaxies with low stellar mass.

3.3. The SFR - O_{32} Relation

In the left panel of Figure 7, we show the O_{32} ratios as a function of SFR for individual galaxies in the NGDEEP final sample and low-SNR sample. We find a general negative correlation between O_{32} and SFR, where O_{32} decreases as SFR increases. The Spearman correlation test returns a correlation coefficient of -0.44 and a p-value of $\sim 10^{-8}$, confirming the significance of the correlation.

We show the median values of the final sample in two redshift bins $1.7 < z < 2.5$ and $2.5 < z < 3.4$ in the left panel of Figure 7. The median values reveal a clear dependence on the redshift with galaxies at higher redshift having higher O_{32} . The negative correlation between O_{32} and SFR and its redshift evolution is consistent with the redshift-dependent SFR- M_* relation and the tight O_{32} - M_* relation.

We quantify the SFR- O_{32} relation for galaxies in the final sample with $M_* > 10^{8.4} M_\odot$ and separated in two

redshift bins with LINMIX (Kelly 2007). We obtain:

$$\begin{aligned} \log(O_{32}) &= (0.37 \pm 0.10) + (-0.27 \pm 0.10) \times \log(\text{SFR}), \\ &\quad (1.7 < z < 2.5) \\ \log(O_{32}) &= (0.72 \pm 0.14) + (-0.36 \pm 0.10) \times \log(\text{SFR}), \\ &\quad (2.5 \leq z < 3.4) \end{aligned} \tag{3}$$

where SFR has units of $M_\odot \text{ yr}^{-1}$. The median intrinsic scatter measured by LINMIX is 0.09 and 0.05 for $z \sim 2$ and $z \sim 3$ fits, respectively. The total scatter of the SFR- O_{32} relations are 0.30 and 0.23 for $z \sim 2$ and $z \sim 3$ fits, respectively. These fits are slightly lower than the median values, particularly at low SFR. This is because the applied mass cut for the fitting excludes some low SFR galaxies, whereas the median values are computed without any mass cut.

We compare our SFR- O_{32} relations to the local and $z \sim 1 - 2$ samples in the right panel of Figure 7. The MOSDEF and CLEAR galaxies are generally consistent with the SFR- O_{32} fit at $z \sim 2$, with an average difference of -0.19 dex and 0.04 dex in O_{32} , respectively. Similar to the mass- O_{32} relation, the SFR- O_{32} relation evolved from $z \sim 0$ from SDSS to $z \sim 1 - 3$ from NGDEEP, CLEAR, and MOSDEF. At fixed SFR, galaxies have a higher O_{32} at higher redshift, and the effect is stronger for galaxies with lower SFR. The O_{32} difference between SDSS and $z \sim 2$ O_{32} -SFR relation are 1.0 dex and 0.7 dex at SFR $1 M_\odot \text{ yr}^{-1}$ and SFR $10 M_\odot \text{ yr}^{-1}$, respectively. Compared to those extreme galaxies at $z \sim 0$, the median O_{32} ratios of CLASSY galaxies lie within our $z \sim 2$ and $z \sim 3$ relations. Green peas and blueberry galaxies on average have higher O_{32} than our $z \sim 3$ and the extended $z \sim 3$ relation, with their median following the upper 1σ total scatter of the $z \sim 3$ relation.

3.4. The sSFR - O_{32} Relation

In the left panel of Figure 8, we show the O_{32} ratios as a function of sSFR for galaxies in the NGDEEP final sample and low-SNR sample. We show the median values for the final sample in two redshift bins $1.7 < z < 2.5$ and $2.5 \leq z < 3.4$. We find a significant positive correlation between the O_{32} ratio and sSFR, with O_{32} increasing as sSFR increases. This is confirmed by a Spearman test with a correlation coefficient of 0.49 and a p-value of $\sim 10^{-10}$. When separating in redshift, the correlation between the O_{32} ratio and sSFR remains significant. The Spearman test returns p-values of $\sim 10^{-8}$ and 0.02 for galaxies at $1.7 < z < 2.5$ and $2.5 \leq z < 3.4$, respectively.

We do not find clear evidence of evolution in the sSFR- O_{32} relation based on the median values of galaxies in

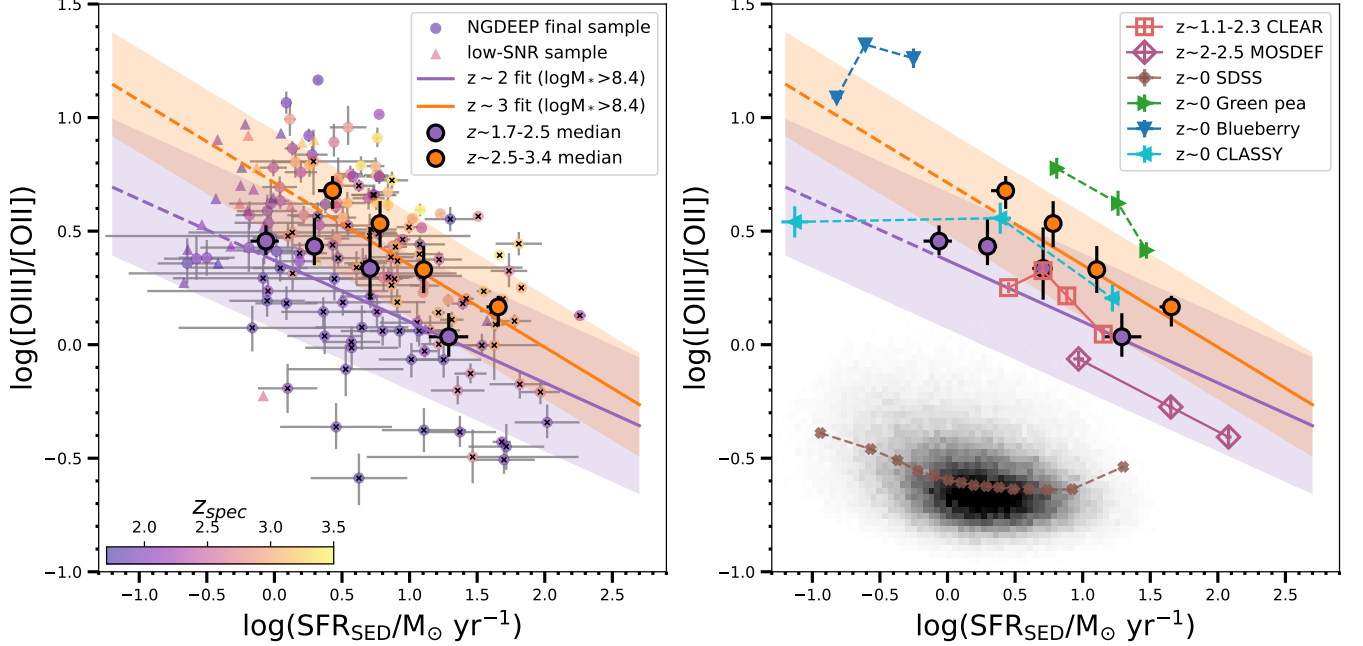


Figure 7. *Left:* The O_{32} versus SFR for galaxies in the NGDEEP final sample (dots) and low-SNR sample (triangle), color-coded by redshift. The median O_{32} values along the abscissa are shown for galaxies at $1.7 < z < 2.5$ and at $2.5 < z < 3.4$ in purple- and orange-filled dots, respectively. The best fit for galaxies with stellar mass $> 10^{8.4} M_{\odot}$ at $z \sim 2$ and $z \sim 3$ are shown as the solid purple and orange lines, and extended to lower SFR as the dashed line. The color-shaded region marks the 1σ total scatter for each redshift sample. *Right:* The median O_{32} ratios as a function of SFR for CLEAR galaxies at $z \sim 1 - 2$ (open orange squares), MOSDEF galaxies at $z \sim 2 - 2.5$ (open magenta diamonds), $z \sim 0$ SDSS galaxies (brown crosses), CLASSY galaxies (cyan triangles), green pea galaxies (green triangles) and blueberry galaxies (blue triangles). The SDSS sample is shown in the 2D histograms in black. The same median values and fits from the NGDEEP O_{32} sample are shown, identical to those in the *left* panel. The NGDEEP sample shows a negative SFR– O_{32} relation, with a dependence on redshift.

two redshift bins. Median values are shifted in sSFR because galaxies at lower redshift are dominated in the relatively lower sSFR region and vice versa. This is most likely due to $z \sim 3$ galaxies following an elevated SFR– M_* relation than that of $z \sim 2$ (see Figure 5).

We quantify the sSFR– O_{32} relation for the final sample with $M_* > 10^{8.4} M_{\odot}$ with LINMIX (Kelly 2007). The fitted sSFR– O_{32} relation is:

$$\log(O_{32}) = (2.19 \pm 0.80) + (0.25 \pm 0.10) \times \log(\text{sSFR}), \quad (4)$$

where sSFR has units of yr^{-1} . The median intrinsic scatter measured by LINMIX is 0.08 dex. The total scatter of the sSFR– O_{32} relation is 0.30 dex. We found consistent slope and intercept of the lines fitted to galaxies at $z \sim 2$ and $z \sim 3$ (including mass cut).

Additionally, we see a diagonal stellar mass gradient as visualized by the color of galaxies with more massive galaxies located in the lower left region, and low-mass galaxies lying in the upper right region. Because of such a mass gradient, the fitted line is consistently lower than the median values across the sSFR range due to the mass cut applied in the fitting.

We compare our sSFR– O_{32} relation to the local and $z \sim 1 - 2$ samples in the right panel of Figure 8. The MOSDEF and CLEAR are generally consistent with the sSFR– O_{32} relation within the 1σ total scatter, with a median difference of -0.21 dex and 0.24 dex, respectively. SDSS galaxies dominate in the low sSFR and low O_{32} region, both lower than $z \sim 2$ galaxies. They lie on the lower envelope of the extended sSFR– O_{32} relation derived from NGDEEP. The median difference between SDSS galaxies and the extended sSFR– O_{32} relation is -0.27 dex and a scatter ranging from -0.44 to -0.01 across the 16th and 84th percentiles. It seems that the O_{32} difference between NGDEEP galaxies at $z \sim 2 - 3$ and SDSS galaxies is smallest at fixed sSFR, compared to the differences at fixed stellar mass or SFR. In particular, the median O_{32} values of SDSS galaxies at $\log(\text{sSFR}) \sim -9$ show consistency with O_{32} of $z \sim 2$ galaxies at the same sSFR.

For those extreme galaxies at $z \sim 0$, the median O_{32} ratios of CLASSY galaxies are located within 1σ of our relations, except the highest sSFR bin. This is most likely due to the same reason described in Section 3.2 that we have a limited number of galaxies at these lower

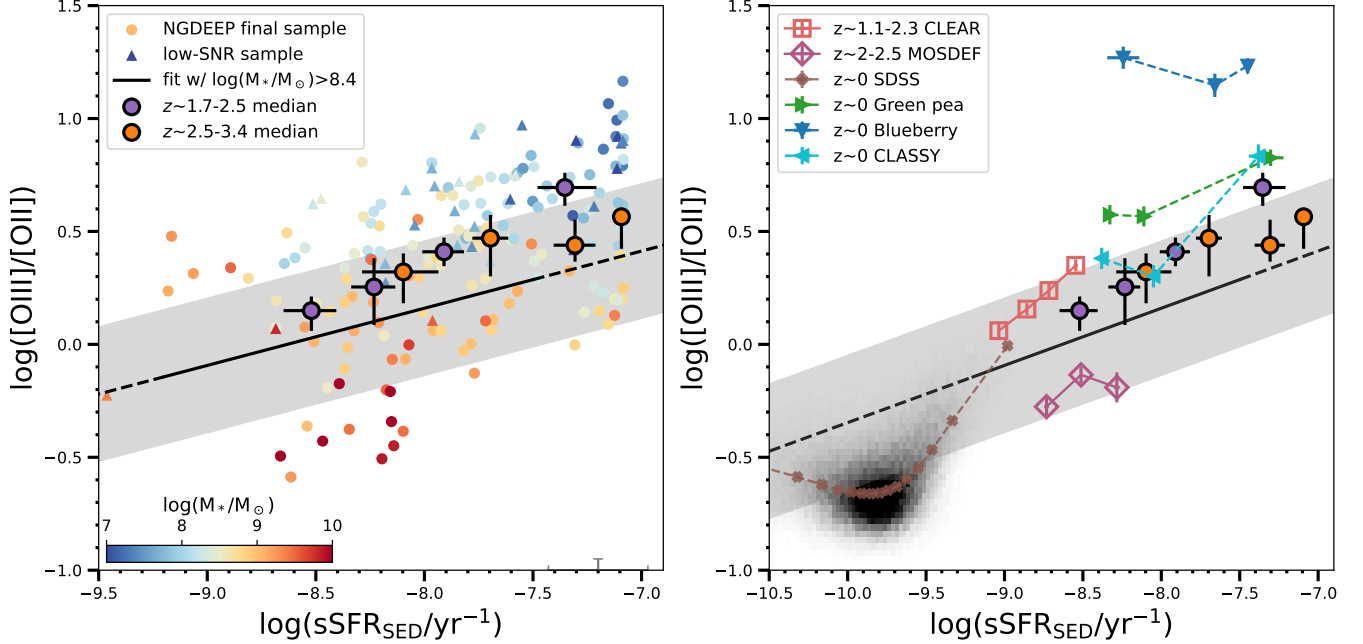


Figure 8. *Left:* The O_{32} versus sSFR for galaxies in the NGDEEP final sample (dots) and low-SNR sample (triangles), color-coded by stellar mass. The median O_{32} values along the abscissa are shown for galaxies at $1.72 < z < 2.5$ and $2.5 < z < 3.4$ in purple- and orange-filled dots, respectively. The best fit for galaxies with stellar mass $> 10^{8.4} M_{\odot}$ and extended to lower/higher sSFR as the dashed line. The grey region marks the 1σ total scatter. *Right:* The median O_{32} ratios as a function of sSFR for CLEAR galaxies at $z \sim 1 - 2$ (open orange squares), MOSDEF galaxies at $z \sim 2 - 2.5$ (open magenta diamonds), $z \sim 0$ SDSS galaxies (brown crosses), CLASSY galaxies (cyan triangles), green pea galaxies (green triangles) and blueberry galaxies (blue triangles). The SDSS sample is shown in the 2D histograms in black. The same median values and fits from the NGDEEP final sample are shown, identical to those in the *left* panel. Note that the x-axis scale of the right panel is more extended. NGDEEP galaxies show a positive sSFR– O_{32} relation without a redshift-dependence between $z \sim 1.7 - 3.4$, but with a large scatter.

stellar masses and high sSFR. Green pea and blueberry galaxies are located well above our sSFR– O_{32} relation, with median offsets of 0.44 dex and 1.03 dex, respectively. They exhibit higher O_{32} values compared to our sample at the same sSFR.

3.5. The $EW - O_{32}$ Relation

We study the distribution of O_{32} with $H\beta$ and $H\alpha$ EW. The EW of $H\beta$ and $H\alpha$ provides an independent method for determining the sSFR, as it is a ratio of $H\alpha$ ($H\beta$) flux, both of which are SFR indicators, to the underlying continuum flux, which traces the stellar mass. In Figure 9, we show the O_{32} ratios as a function of $EW(H\beta)$ and $EW(H\alpha)$ for galaxies in the NGDEEP final sample and the low-SNR sample with $H\beta$ and $H\alpha$ SNR > 5 , respectively. We find significant positive correlations between O_{32} and $EW(H\beta)$, and O_{32} and $EW(H\alpha)$. These are confirmed by a Spearman test with a correlation coefficient of 0.70 and 0.77 for the two relations, respectively, and p-values of $\sim 10^{-18}$ for both.

We quantify the EW – O_{32} relation for the NGDEEP final sample with $M_* > 10^{8.4} M_{\odot}$ with LINMIX (Kelly

2007) as following:

$$\log(O_{32}) = (-1.09 \pm 0.23) + (0.75 \pm 0.13) \times \log(EW(H\beta)), \quad (5)$$

$$\log(O_{32}) = (-1.56 \pm 0.41) + (0.74 \pm 0.17) \times \log(EW(H\alpha)), \quad (6)$$

where $EW(H\beta)$ and $EW(H\alpha)$ are in rest-frame with units of \AA , where the median intrinsic scatter is 0.05 and 0.07, respectively, measured by LINMIX. The total scatter of the $EW(H\beta)$ – O_{32} and $EW(H\alpha)$ – O_{32} relations are 0.24 and 0.26, respectively. For the $EW(H\beta)$ – O_{32} relation, we do not find any significant redshift evolution. Similar to sSFR– O_{32} relation, we see a diagonal stellar mass gradient, where, at a fixed EW (or sSFR), more massive galaxies have lower O_{32} ratios.

In the right panels of Figure 9, we compare our EW – O_{32} relations to the local and $z \sim 1 - 2$ samples that have available EW measurements. The CLEAR galaxies show an $EW(H\beta)$ – O_{32} relation consistent with ours, with a small median difference of 0.04 dex. SDSS galaxies mostly occupy the low O_{32} and low EW region, with a tail of high EW and high O_{32} galaxies that tend to

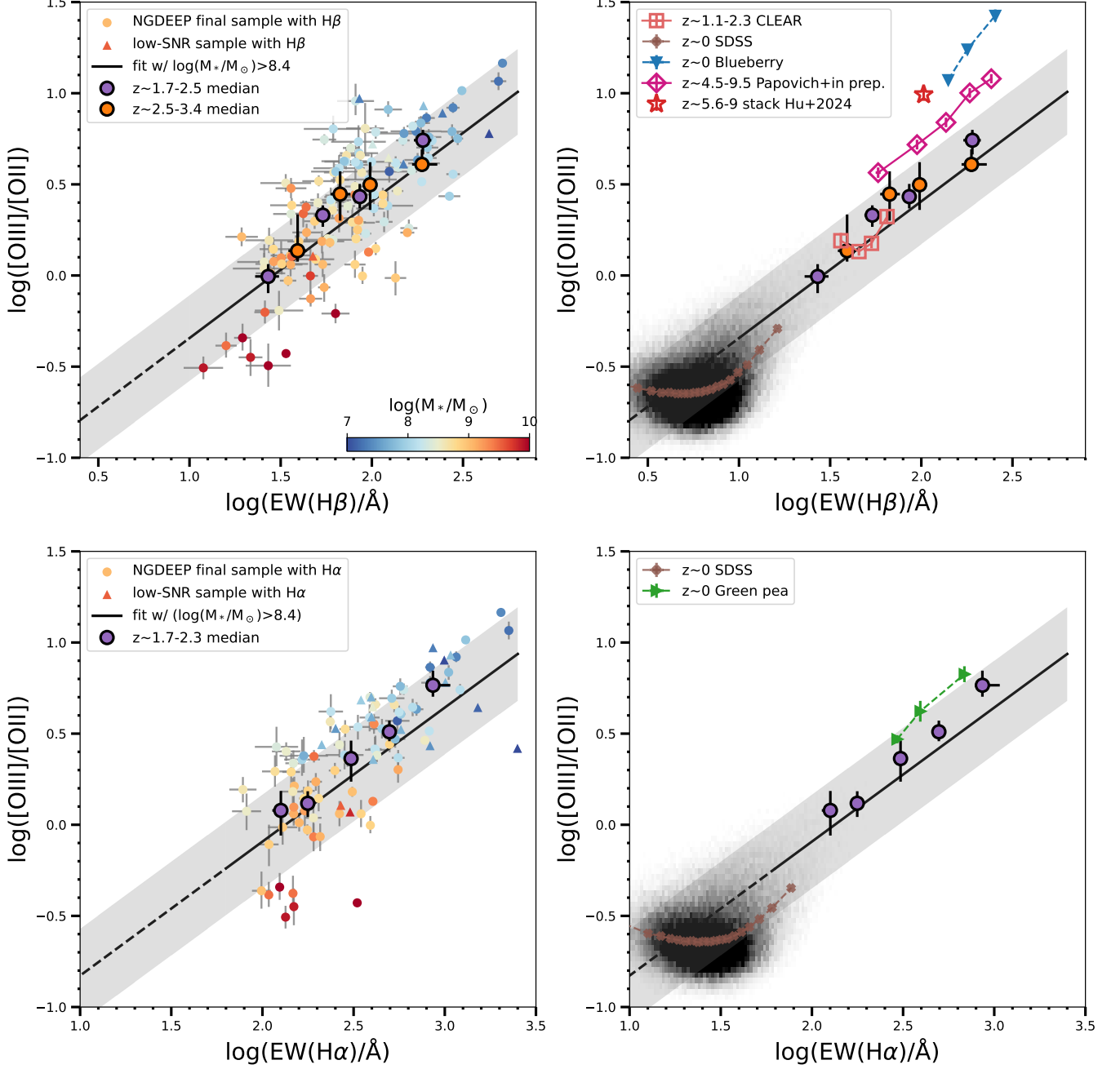


Figure 9. *Lefts:* The relation between the O_{32} ratio and $H\beta$ EW (*top*) and $H\alpha$ EW (*bottom*) for galaxies in the NGDEEP final sample and low-SNR sample with $H\beta$ and $H\alpha$ $SNR > 5$, respectively. Individual galaxies are color-coded by stellar mass. The median O_{32} values are shown for galaxies at $1.7 < z < 2.5$ and $2.5 \leq z < 3.4$ as black orange-filled and purple-filled dots, respectively. The best fit for galaxies in the final sample with $M_* > 10^{8.4} M_\odot$ is shown as the solid black line and extended to the low EW region as the dashed black line. *Rights:* Comparison with galaxy samples at different redshift ranges. Median O_{32} ratios are shown for galaxies at $z \sim 4.5 - 9.5$ from CEERS and JADES (Papovich et al. *in prep.*, open magenta diamonds), galaxies at $z \sim 5.6 - 9$ measured from composite spectra (Hu et al. 2024, red star), CLEAR galaxies at $z \sim 1.1 - 2.3$ (open orange squares), $z \sim 0$ SDSS galaxies (brown crosses), blueberry galaxies (blue triangles), green pea galaxies (green triangles). The SDSS sample is shown in black as the 2D histogram. The same median values and fits from the NGDEEP final sample are shown, identical to those in the *left* panel. The NGDEEP sample shows tight EW- O_{32} relations. A clear evolutionary trend is seen as higher redshift galaxies having higher sSFR and O_{32} .

align with our $z \sim 2-3$ EW–O₃₂ relation. We measured a relatively small difference between SDSS and our extended EW–O₃₂ relations, with a median difference of -0.06 and -0.07 for the EW(H β) and EW(H α) relations, respectively. These offset values, both for SDSS and CLEAR, are much smaller than those from sSFR–O₃₂ comparison, likely due to the different methods used for SFR measurements, while EW are all calculated in a similar way and account for stellar absorption. Green pea and blueberry galaxies are located above our EW–O₃₂ relation, with median offsets of 0.2 dex and 0.6 dex, respectively. However, these samples were selected to be extreme emission-line galaxies, which likely accounts for their offsets.

Furthermore, we compare galaxies at $z \gtrsim 5$ with our EW–O₃₂ relation. Firstly, we include 232 galaxies with [O II], [O III], and H β emission line fluxes SNR > 3 measured using the *JWST* PRISM data taken as part of CEERS and JADES surveys (Papovich et al. *in prep.*). The median dust-corrected O₃₂ ratios as a function of EW(H β) are shown in the top right panel of Figure 9. Secondly, we include the O₃₂ ratio and EW(H β) obtained based on the composite spectrum of 63 galaxies at $5.6 < z < 9$ using the *JWST* medium resolution grating spectra (M-Grating) from CEERS and JADES survey (Hu et al. 2024). Note that this EW(H β) might be underestimated, due to some systematic background issues shown in the composite spectrum (see Figure 2 in Hu et al. 2024 and more discussion there). These $z \gtrsim 5$ galaxies dominate in the high EW H β region. The median O₃₂ of $z \gtrsim 5$ galaxies lie above our $z \sim 2-3$ relations with a median difference of 0.36 dex. We find an evolutionary trend in O₃₂ and EW(H β) from $z \sim 0$ to $z \gtrsim 5$ that as higher redshift galaxies have higher EW(H β) and higher O₃₂. These $z \gtrsim 5$ galaxies seem to occupy a region similar to green pea galaxies and blueberry galaxies, suggesting they have similar star formation and ISM properties (i.e., ionization parameter and metallicity).

4. DISCUSSION

We compared the O₃₂ ratio with galaxy properties including stellar mass, SFR, sSFR, and EW of H α and H β for NGDEEP galaxies at $z \sim 1.7-3.4$ in the final sample (i.e., those galaxies with [O II] and [O III] > 5 σ detections). The O₃₂ ratio increases with (1) decreasing stellar mass, (2) decreasing SFR, (3) increasing sSFR, and (4) increasing EW of H α and H β . We quantify the significance and scatter of these relations in Table 3.

The NGDEEP final-sample galaxies at $z \sim 2-3$ have on average higher O₃₂ compared to local normal star-forming galaxies from SDSS at the same stellar mass and SFR. This is consistent with other findings for galaxies at $1 \lesssim z \lesssim 3$ (Sanders et al. 2016; Papovich et al. 2022). The $z \sim 2-3$ galaxies also have higher sSFR values than local galaxies, a manifestation of “downsizing”. On the other hand, $z \sim 2-3$ galaxies have similar to lower O₃₂ than those of extreme local galaxies from low-redshift samples such as CLASSY, and the SDSS Green pea, and blueberry galaxies at fixed stellar mass, SFR, sSFR, and EW. Therefore these local samples are more typical of the high-O₃₂ tail of the high-redshift samples than of the typical galaxy in the NGDEEP final sample.

Our NGDEEP sample spans a wide range of O₃₂, stellar mass, and sSFR (or EW), extending to lower stellar masses and higher sSFR than previously studied at these redshifts (our sample extends to $M_* \sim 10^7 M_\odot$). This helps bridge the gap between the local galaxies and galaxies at $z > 5$. Compared to the higher redshift galaxies, we find an evolutionary trend in EW(H β) – O₃₂ from $z \sim 0$ to $z \gtrsim 5$. Higher redshift galaxies have higher O₃₂ at fixed EW(H β) (see Figure 9). However, the evolutionary trend in the EW(H β)–O₃₂ relation is mild, as the difference between the O₃₂ ratios for the NGDEEP galaxies and SDSS galaxies is the smallest at fixed EW. This contrasts with the strong evolution in O₃₂ at fixed stellar mass, SFR, or sSFR. This merits future study to understand how this connects to the physical properties of the galaxies as a function of redshift, which we will explore in a future paper.

Figure 8 and 9 show a positive correlation between the O₃₂ ratio and sSFR, EW(H α) and EW(H β), consistent with previously at low and high redshifts (e.g., Nakajima & Ouchi 2014; Kewley et al. 2015; Sanders et al. 2016; Bian et al. 2016; Kaasinen et al. 2018; Kashino et al. 2019; Papovich et al. 2022). We found that the scatter of EW–O₃₂ relation is smaller than that of the sSFR–O₃₂ relation. This is explainable as EW and O₃₂ are all calculated using nebular emission lines originating from the same regions. The EW–O₃₂ correlation indicates a close connection between O₃₂ and the star formation history on $\sim 5-10$ Myr timescales, to which the H α and H β are sensitive. In contrast, the SFR from the SED fitting is primarily based on the UV luminosity and is sensitive to changes in the star-formation history on ~ 100 Myr timescales. The fact that the EW–O₃₂ correlation exists implies it is related to the SFR on these short timescales.

The O₃₂ ratio is sensitive to the ionization parameter. Papovich et al. (2022) found a tight correlation between O₃₂ and ionization parameter derived by modeling the [O II], [O III], and H β of the CLEAR galaxies with the

Table 3. Summary of correlations between O_{32} and galaxies properties

Galaxy Properties	redshift range ^a	c_1^b	c_0^b	intrinsic scatter ^c	total scatter ^d	p-value ^e
M_*		-0.47 ± 0.06	4.44 ± 0.53	0.04	0.23	10^{-32}
SFR		-0.22 ± 0.08	0.42 ± 0.08	0.09	0.30	10^{-32}
SFR	$1.7 < z < 2.5$	-0.27 ± 0.10	0.37 ± 0.10	0.08	0.28	10^{-4}
SFR	$2.5 \leq z < 3.4$	-0.36 ± 0.10	0.72 ± 0.14	0.05	0.23	10^{-11}
sSFR		0.25 ± 0.10	2.19 ± 0.80	0.08	0.30	10^{-10}
EW(H β)		0.75 ± 0.13	-1.09 ± 0.23	0.05	0.23	10^{-19}
EW(H α)	$1.7 < z < 2.3$	0.74 ± 0.17	-1.56 ± 0.41	0.07	0.26	10^{-17}

NOTE—^a The redshift range is $1.7 < z < 3.4$ if not specified. Only the SFR– O_{32} relation shows a redshift dependence, so we separate the SFR– O_{32} relation in two redshift bins. The EW(H α)– O_{32} relation is restricted to galaxies at $1.7 < z < 2.3$ as our NIRISS data cover H α emission line up to $z = 2.3$.

^b $\log O_{32} = c_0 + c_1 \times x$, where x is the galaxies properties in logarithm.

^c The median intrinsic scatter measured from LINMIX, in a unit of dex.

^d The total scatter measured from the fitted relation, in a unit of dex.

^e The p-value is measured from the Spearman rank correlation test.

MAPPINGS V photoionization models (Sutherland & Dopita 1993; Dopita & Sutherland 1996). They also found a secondary effect that some of the galaxies with high O_{32} ratio shift below the O_{32} –ionization relation, likely due to the effect of metallicity (Strom et al. 2018). This metallicity dependence has been previously seen in photoionization models Kewley et al. (2013), and the existence of anti-correlation between O_{32} and metallicity up to $z \sim 9$ (e.g., Maiolino et al. 2008; Jones et al. 2015; Sanders et al. 2024). Because the O_{32} ratio has a dependence on metallicity, the evolution in the relation between O_{32} and galaxy properties would be a consequence of, or largely driven by, the evolution of the mass–metallicity relation (e.g., (Erb et al. 2006; Maiolino et al. 2008; Zahid et al. 2011, 2014; Sanders et al. 2018; Curti et al. 2020; Sanders et al. 2021)).

In the remainder of this section, we consider potential biases in our results, and we explore the implications of some of the trends further. As mentioned above (Section 2.6), all galaxies in the NGDEEP full sample have [O III] detections above 5σ , which potentially introduces selection bias. We investigate this further and discuss any potential impacts on our results in Section 4.1. We explore the dependence of the O_{32} ratio on ionization parameter and metallicity in Section 4.2. Finally, we discuss the effect on ionization parameters that drives the changes in the O_{32} ratio in Section 4.3.

4.1. Testing for Selection Bias

During the sample selection (see Section 2.6), we first choose galaxies with reliable redshift from the NIRISS grism data. Because [O III] is the strongest emission line in our sample, we primarily rely on its detection for the

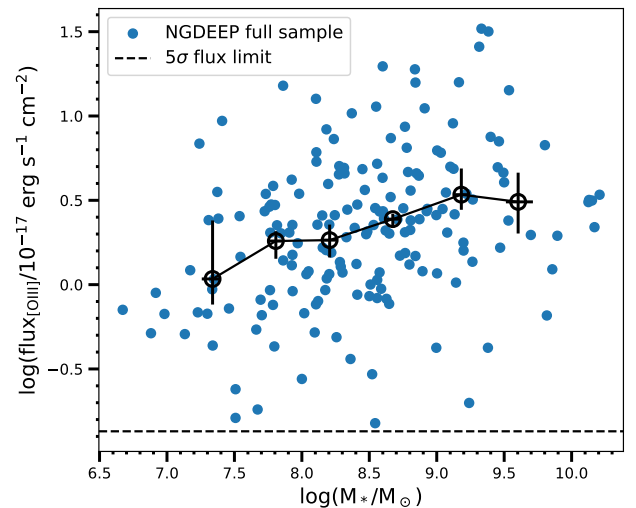


Figure 10. The [O III] emission-line flux versus stellar mass for the NGDEEP full sample (blue dots). Median values are shown in open black dots connected by black lines. The 5σ flux limit estimated using all emission lines is plotted as a horizontal dashed line (see Section 2.2). Above the mass completeness limit ($\log(M_*/M_\odot)=8.4$), no significant bias is found.

redshift determination. However, this approach may introduce a selection bias as it could limit our detection of galaxies with fainter [O III] emission. Figure 10 shows the distribution of [O III] flux as a function of stellar mass for the NGDEEP full sample compared to our limiting flux limit. While there is a very mild trend that the [O III] emission-line flux increases slowly with increasing stellar mass (the median [O III] fluxes increase by $\simeq 0.11$ dex from $\log(M_*/M_\odot) = 8.4$ to 10), the median is well

above our detection limit. Thus, above our mass completeness limit ($\log(M_*/M_\odot)=8.4$), we do not see any evidence that we are missing a significant population of objects with low [O III] fluxes.

With this said, our sample selection also requires that galaxies have rest-frame UVJ colors that classify them as “star-forming” (see Section 2.6 and Table 2). Therefore our sample, by construction, is devoid of quiescent galaxies at these stellar masses and redshifts, which likely contain objects with low or absent nebular emission. Our results therefore apply only to the star-forming population.

Our sample is biased to higher SFRs at fixed stellar mass compared to measurements of the SFMS at the same redshifts (see Section 3.1 and Figure 5). This bias is likely related to the fact that our sample is based on emission-line selection, while most measurements of the SFMS used photometric bands with color-selection of star-forming galaxies (e.g., Whitaker et al. 2014; Tomczak et al. 2016). We also note that the SFR values are calculated in different methods that we adopt SFR from SED fitting and well-matched with $H\alpha$ -derived SFR, while, Whitaker et al. (2014) adopted SFR calculated from modeling the broadband imaging from the rest-frame UV to mid/far-IR.

4.2. The Dependence of O_{32} on Ionization Parameter and Metallicity

To investigate the O_{32} ratio dependence on ionization parameter and metallicity, we applied the Python version of code “Inferring the gas-phase metallicity (Z) and Ionization parameter” (IZI, Blanc et al. 2015) developed by Mingozi et al. (2020) to our dataset. IZI is a Bayesian code that computes posterior likelihoods for the gas-phase metallicity and the ionization parameter by comparing the measured emission line fluxes to predictions from the photoionization models. Based on the original IZI, the new Python version adds the option of using a more efficient Markov-chain Monte-Carlo (MCMC) algorithm and simultaneously fits the dust attenuation following the Calzetti et al. (2000) extinction law. However, the dust-attenuation modeling requires coverage of both $H\beta$ and $H\alpha$, while [O II], [O III], and $H\beta$ are the minimum needed to constrain metallicity and the ionization parameter. For the 64 galaxies in the NGDEEP final sample with all four emission lines ([O II], [O III], $H\beta$, and $H\alpha$ + [N II]) detected with $\text{SNR} > 5$, we use the MCMC algorithm. For the 55 galaxies in the NGDEEP final sample only with [O II], [O III], and $H\beta$ $\text{SNR} > 5$, we use the original IZI algorithm and the dust-corrected fluxes following Section 2.4.

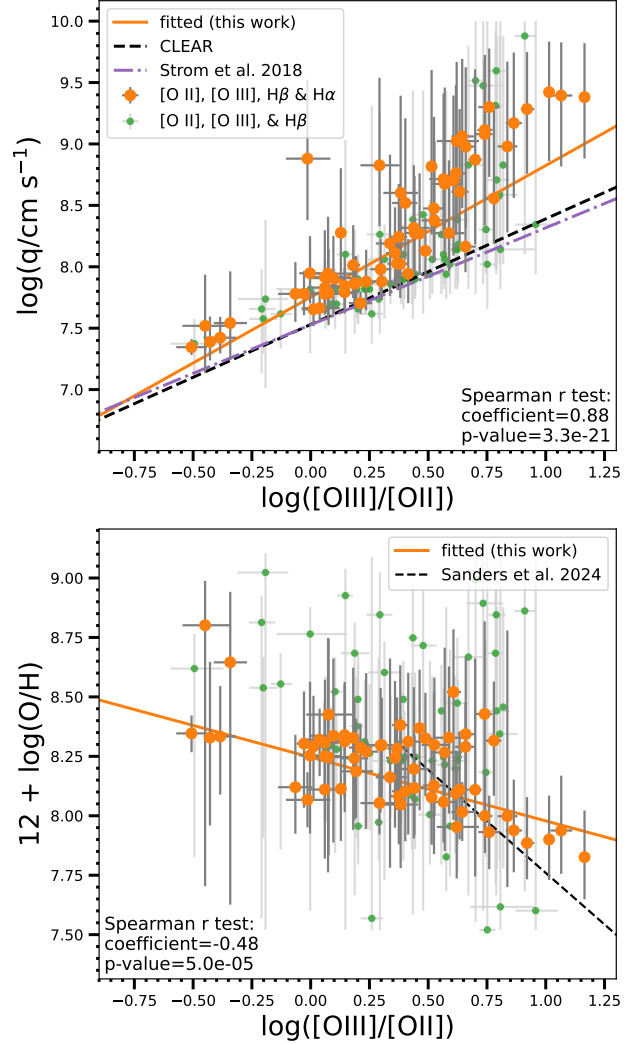


Figure 11. The distribution of ionization parameter q (*top*) and metallicity ($12+\log(O/H)$, *bottom*) as function of O_{32} . Galaxies with all four emission lines $> 5\sigma$ and with three lines ([O II], [O III], and $H\beta$) $> 5\sigma$ are shown in orange and green, respectively. The orange solid lines show a linear fit to the NGDEEP galaxies with all four emission line detection. The *top* panel shows the relations from CLEAR galaxies (Papovich et al. 2022) (black dashed line) and a sample of $z \sim 2.3$ SFGs from Strom et al. (2018) (purple dashed line). The *bottom* panel shows the relation derived from a sample of $z \sim 2-9$ galaxies from Sanders et al. (2024) (black dashed line). While O_{32} correlates with both ionization parameter and metallicity, the relationship between O_{32} and the ionization parameter is more pronounced.

For the photoionization models, we adopt the MAPPING V grid models (Kewley et al. 2019b,a). We generated isobaric models with the ISM pressure of $\log(P/k)[\text{K cm}^{-3}] = 7$, a grid of ionization parameters $\log(q)$ [cm s^{-1}] from 6 to 10 in intervals of 0.25, and a grid of metallicities (Z) with [0.05, 0.2, 0.4, 1.0] Z_\odot

(Jung et al. 2024). The choice of ISM pressure is motivated by the combination of median electron density, $n_e \sim 250 - 300 \text{ cm}^{-3}$ for galaxies at $z \sim 2 - 3$ (Sanders et al. 2016; Strom et al. 2017) and the nebular temperature of $\sim 10,000\text{-}20,000\text{K}$ (Sanders et al. 2020). We also tested models with $\log(P/k) = 6.5$ and $\log(P/k) = 7.5$. Adopting these models does not alter our conclusions.

We show the ionization parameter as a function of O_{32} for our NGDEEP final sample in the top panel of Figure 11. The ionization parameter increases as O_{32} increases. The Spearman correlation test returns a correlation coefficient of 0.88 and a p-value of $\sim 10^{-21}$ with all four emission lines, and a p-value of $\sim 10^{-33}$ when including galaxies with three emission lines.

We fit a linear relation between $\log(O_{32})$ and $\log(q)$ for galaxies with all four emission lines using LINMIX:

$$\log q = (7.75 \pm 0.04) + (1.06 \pm 0.11) \times \log(O_{32}) \quad (7)$$

where the ionization parameter, q , is in the units of cm s^{-1} . The total scatter of the O_{32} - q relation is 0.35 dex. However, at high O_{32} , galaxies have higher $\log(q)$ values than predicted by the linear fit (this occurs primarily at $\log(O_{32}) > 0.75$, see Figure 11). Interestingly, all six of these galaxies (with $\log(O_{32}) > 0.75$) have near-zero dust attenuation with $E(B - V) < 0.05$. These galaxies all have Balmer decrements *lower* than the Case B value of $H\alpha/H\beta = 2.86$ (see Figure 3 and Section 2.5). This forces IZI to increase the ionization parameter to model the emission line ratios to account for the low $E(B - V)$. We show the 1D spectra of two examples of these galaxies and their PDFs from IZI in Figure 12. Finally, removing them does not quantitatively change our result given their large uncertainties.

This linear fit is steeper than those obtained from other studies at these redshifts (Strom et al. 2018; Papovich et al. 2022). This difference mostly appears in the high O_{32} region, where the majority of galaxies from Papovich et al. (2022) and Strom et al. (2018) do not extend to these high O_{32} ratios. Additionally, this difference could be due to the selected range of ionization parameters. Papovich et al. (2022) derived their relation from the CLEAR sample, also using space-based slitless grism data but at a slightly lower redshift. They used the original IZI code with MAPPINGS IV photoionization models with $\log(q)$ spanning the range of 6.5 to 8.5. However, only one of the sources in their sample had $\log(O_{32}) > 0.75$, and those authors noted that at high O_{32} the modeling favored higher ionization parameter. Strom et al. (2018) derived their relation from a sample of $z \sim 2.3$ SFGs with independent photoionization modeling with $\log(q)$ spanning the range of 7 to 9. When we use models with the range of $\log(q)$ from

6.5 to 8.5, we recover the same trend as Papovich et al. (2022) and Strom et al. (2018). However, when we used this limited $\log(q)$ range ($\log(q) \sim 6.5 - 8.5$), the fitted $\log(q)$ for galaxies with $\log(O_{32}) \gtrsim 0.75$ show that show a skewed probability distribution function towards the upper limit, and with their mode approaching $\log(q) = 8.5$. Therefore, our results suggest the linear relation between O_{32} and the ionization parameter breaks down at high values of this ratio, $O_{32} \gtrsim 0.75$,

We show the metallicity as a function of the O_{32} ratio for our NGDEEP final sample in the bottom panel of Figure 11. The metallicity decreases with O_{32} increases. The Spearman correlation test returns a correlation coefficient of -0.43 and a p-value of $\sim 10^{-4}$ with all four emission lines and a p-value of 0.001 when including galaxies with three emission lines.

We quantified the (anti-)correlation between $\log(O_{32})$ and $12 + \log(O/H)$ using galaxies with all four emission lines ($[O \text{ II}]$, $[O \text{ III}]$, $H\beta$, and $H\alpha + [N \text{ II}]$) using LINMIX:

$$12 + \log(O/H) = (8.24 \pm 0.04) + (-0.27 \pm 0.07) \times \log(O_{32}), \quad (8)$$

where the 1σ scatter is 0.17 dex. Our fitted linear relation is flatter than that from Sanders et al. (2024), who derived their relation using metallicity from the direct T_e method from a sample of galaxies at $z \sim 2 - 9$. However, our data points are scattered around their fit at high O_{32} region or low metallicity regions. Our sample extends to low O_{32} region where Sanders et al. (2024) did not cover, while this region predominantly drives our fit. Overall, our results suggest that the O_{32} ratio is a strong tracer of gas ionization parameter, with a secondary dependence on metallicity.

The tight mass- O_{32} relation with a scatter of 0.21 dex is difficult to explain by the scatter of O_{32} -metallicity calibrations (~ 0.29 dex from Sanders et al. 2024 and 0.28 dex from our data) and the scatter of mass-metallicity relation (~ 0.14 dex from Sanders et al. 2021). This scatter is also revealed from the distribution of O_{32} and $R_{23} \equiv ([O \text{ III}] + [O \text{ II}]/H\beta)$ which is sensitive to the gas-phase metallicity (Nakajima & Ouchi 2014; Sanders et al. 2016; Papovich et al. 2022). Although, we cannot rule out the possible effect of the metallicity on the mass-, SFR- and sSFR- O_{32} relations, the ionization parameter may play a more important role in these O_{32} - galaxy properties relations.

4.3. The Relation between the $[O \text{ III}]/[O \text{ II}]$ Ratio, Ionization Production, and SFR

As the O_{32} ratio primarily depends on the ionization parameter, in this section, we focus on the possible effect on the ionization parameter that drives the changes in the O_{32} ratio. The ionization parameter is, by definition,

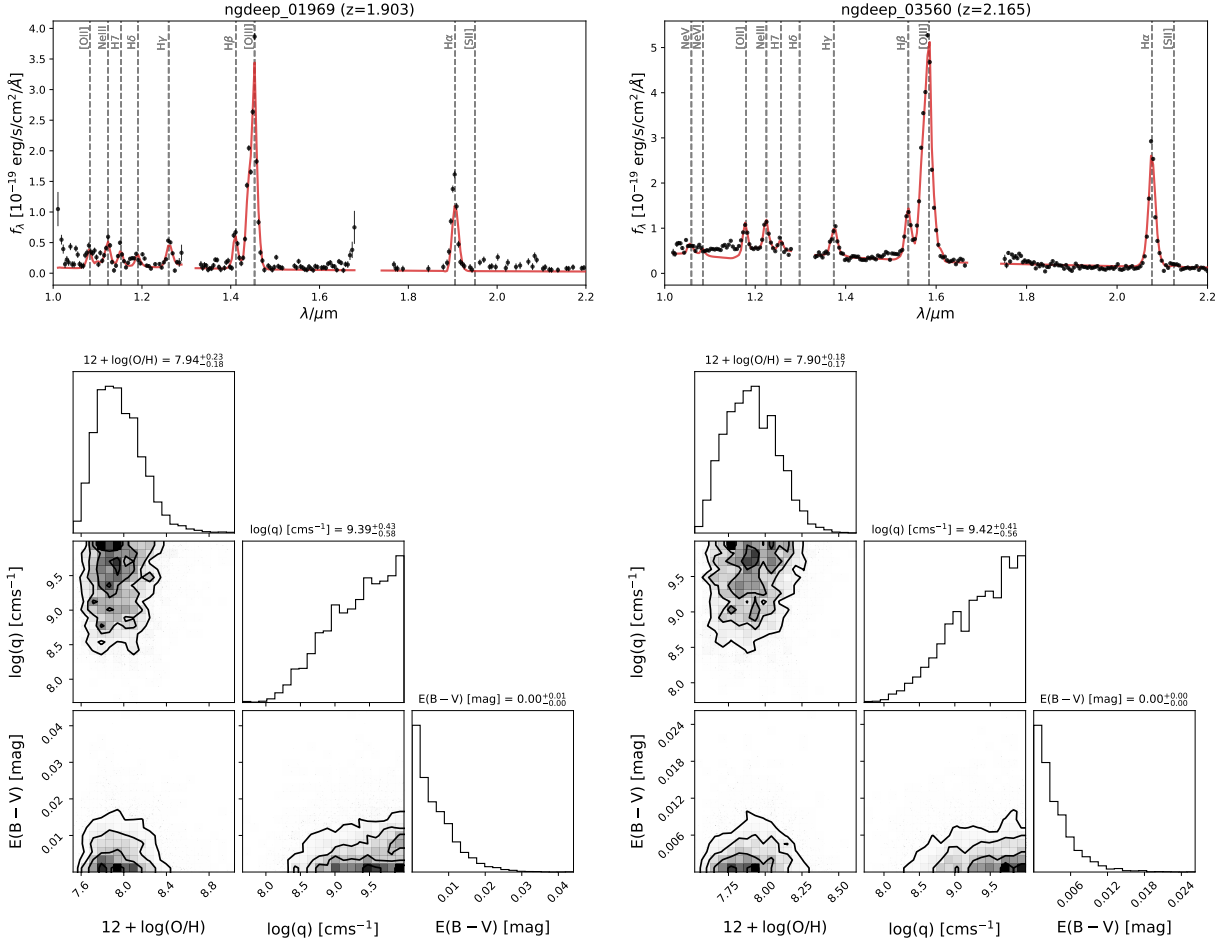


Figure 12. *Top:* 1D spectrum of two galaxies with $\log(\text{O}_{32}) > 0.75$ and $|\text{ZI}|$ -derived $E(B-V) \simeq 0$. Each panel shows the NIRISS grism data (black dots) along with the best-fit spectrum (red line). Important emission lines are marked by vertical grey dashed lines. *Bottom:* The corner plot of $12 + \log(\text{O}/\text{H})$, $\log(q)$, and $E(B-V)$ from $|\text{ZI}|$ for the same galaxies as *top* panel. The median and associated uncertainties are displayed on the top of the histograms.

the ratio of the hydrogen ionizing photon flux and the density of hydrogen atoms. For a radiation-bounded nebula, the average ionization parameter can be written as:

$$q = \left(\frac{3Qn_{\text{H}}\epsilon\alpha_B^2}{4\pi} \right)^{1/3} \quad (9)$$

where Q is the ionizing photon production rate, α_B is the case-B hydrogen recombination coefficient, n_{H} is the number density of hydrogen, and ϵ is the volume filling factor of the gas. Here, we assume no change in α_B and ϵ for galaxies with different SFR and M_* and across redshift (see more discussion in Papovich et al. 2022). Thus, the ionization parameter in this case depends only on Q and n_{H} .

4.3.1. Ionizing photon production rate

The ionizing photon production rate depends on the properties of massive stars, their evolution, and the IMF. We estimate the ionizing photon production rate

Q following Leitherer & Heckman (1995) and assuming an ionizing photon escape fraction of zero:

$$Q = 7.35 \times 10^{11} L(\text{H}\alpha) [\text{s}^{-1}] \quad (10)$$

where the $L(\text{H}\alpha)$ is the dust-corrected $\text{H}\alpha$ luminosity in units of erg s^{-1} . We also adopt the ionizing production efficiency ξ_{ion} defined as the ionizing photon production rate per unit UV luminosity, as follows:

$$\xi_{\text{ion}} = \frac{Q}{L(\text{UV})} [\text{s}^{-1}/\text{erg s}^{-1} \text{Hz}^{-1}] \quad (11)$$

where $L(\text{UV})$ is the intrinsic UV luminosity at rest-frame 1500 Å. We adopt the rest-frame FUV luminosity from CIGALE SED fits for each galaxy in our sample and convert it to intrinsic UV luminosity by correcting the dust with $E(B-V)_{\text{star}}$ from SED fitting and following the Calzetti et al. (2000) law (see more details in Section 2.4).

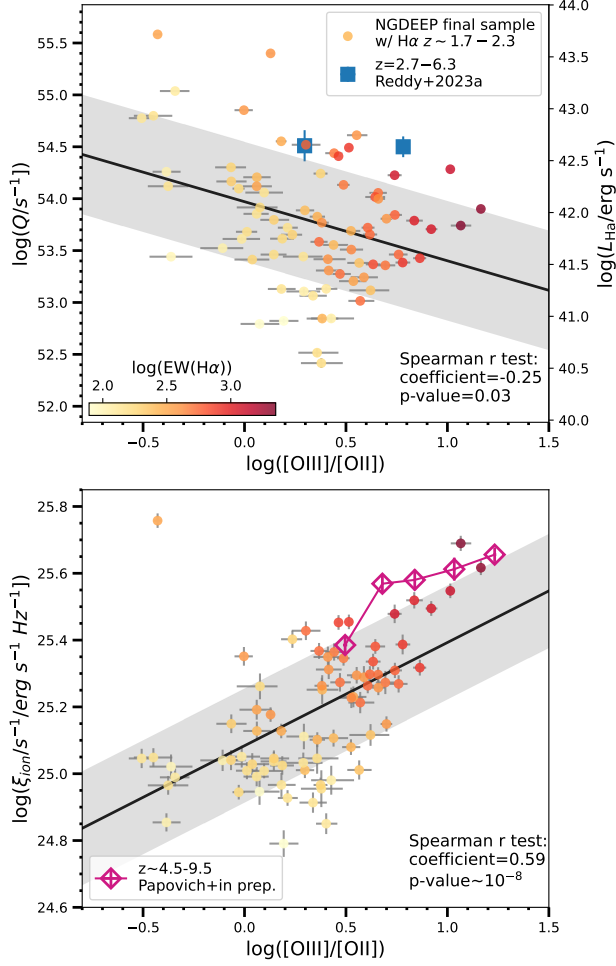


Figure 13. The distribution of O_{32} and ionizing photon production rate Q (*top*) and ionizing production efficiency ξ_{ion} (*bottom*) for the NGDEEP final sample with $\text{H}\alpha$ SNR > 5 , color-coded by $\text{EW}(\text{H}\alpha)$. The best fits for the NGDEEP O_{32} galaxies (without mass cut) are shown as the solid black lines and 1σ total scatter is shown as the grey regions. The median values of galaxies at $z = 2.7 - 6.3$ from Reddy et al. (2023a) are shown as blue squares in the top panel. The median values of galaxies at $z \sim 4.5 - 9.5$ from CEERS and JADES (Papovich et al. *in prep.*) are shown in open magenta diamonds. The ionizing production efficiency could be one of the contributions to increasing O_{32} .

In the top panel of Figure 13, we show the distribution of the Q and ξ_{ion} values as a function of O_{32} for the NGDEEP final sample with $\text{H}\alpha$ SNR > 5 . There is a weak negative correlation between O_{32} and Q with a Spearman rank correlation coefficient of -0.25 and a p-value of 0.03. Because Q depends only on $\text{H}\alpha$ luminosity, which also traces the SFR (also see Figure 2), Q versus O_{32} is similar to the SFR versus O_{32} as shown in Figure 7. The scatter of the fitted O_{32} - Q relation is large with a value of 0.58 dex, consistent with the large

scatter on the SFR- O_{32} relation. This result suggests that an increase in the ionizing photon production rate, Q , has little impact on the O_{32} ratio. This is consistent with the findings of Reddy et al. (2023a), who studied a sample of 48 SFGs at $z = 2.7 - 6.3$ with O_{32} spanning a range of 0.5 – 100. They found no correlation between the ionizing photon production rate between low- and high- O_{32} galaxies with mean O_{32} values of 1.98 and 6.06, respectively, as shown in Figure 13. Their mean Q values are higher than the trend derived from our sample at fixed O_{32} , which could be due to their sample containing galaxies at higher redshift.

In the bottom panel of Figure 13, we find a positive correlation between O_{32} and ξ_{ion} such that ξ_{ion} increases with increasing O_{32} . The Spearman rank correlation test confirms the significance of this relation, with a correlation coefficient of 0.59 and a p-value of $\sim 10^{-8}$. The correlation means that the O_{32} ratio is a strong predictor of the ionizing production efficiency. The scatter is also non-negligible, 0.17 dex. This could be related to the star formation history. The ξ_{ion} values are calculated using the $\text{H}\alpha/\text{UV}$ ratio, which is commonly used as a tracer for recent bursty star-formation activity (e.g., Emami et al. 2019; Guo et al. 2016; Faisst et al. 2019). An elevated $\text{H}\alpha$ emission with respect to the UV continuum is a sign of bursty star-formation activity in the past ~ 10 Myr. Similarly, the $\text{EW}(\text{H}\alpha)$ and sSFR are sensitive to recent star-formation activity. The difference between $\text{EW}(\text{H}\alpha)$ and $\text{H}\alpha/\text{UV}$ ratio is their denominator: the stellar continuum flux and UV continuum flux, respectively. The UV continuum flux traces SF activity in the recent 100-200 Myr. Thus, the two measurements are comparable for a galaxy with an age less than ~ 100 -200 Myr or a galaxy with a constant star formation history. Therefore, it is not surprising that a correlation between ξ_{ion} and sSFR exists for high redshift galaxies up to $z \sim 7$ (Faisst et al. 2019; Emami et al. 2020; Endsley et al. 2021; Emami et al. 2020; Prieto-Lyon et al. 2023) and for extreme galaxies at lower redshift $z \sim 1$ (Tang et al. 2019; Izotov et al. 2021). In Section 3.4, we found O_{32} is correlated with sSFR and $\text{EW}(\text{H}\alpha)$. Here we find that O_{32} is correlated with ionizing production efficiency, confirming the connection between ionization parameters and recent star-formation activity.

In addition, we compare galaxies at $z \sim 4.5 - 9.5$ from Papovich et al. (*in prep.*) with our O_{32} - ξ_{ion} relation. The median ξ_{ion} of $z > 5$ galaxies generally follows our relation but is offset to slightly higher ξ_{ion} at fixed O_{32} . The higher ξ_{ion} could be due to a recent starburst which increases the number of massive young stars and boosts the production of ionizing photons. This is consistent

with the comparison of $\text{EW}(\text{H}\beta)\text{--}\text{O}_{32}$ relation where the $z > 5$ galaxies tend to have higher $\text{EW}(\text{H}\beta)$ than our NGDEEP galaxies at $z \sim 2 - 3$ (see Figure 9). It is unclear what causes the shift toward higher ξ_{ion} with increasing redshift, though we expect it could be due to low metallicity as metal-poor stars are hotter and more efficient at generating ionizing radiation.

One galaxy (NGDEEP_02938) is significantly offset from the fitted relation, with very high ionizing production efficiency, ξ_{ion} , and relatively low O_{32} ratio. We conclude this offset is likely linked to the fact that it has the highest $E(B - V)$ in our sample, with $E(B - V) = 1.13$ from Balmer decrement and $E(B - V)_{\text{star}} = 0.48$ from SED fitting. These values correspond to an attenuation of $A_V \gtrsim 1.5$, and an optical depth of $\tau \gtrsim 1.6$, indicating the galaxy is optically thick. Due to the optical thickness, the UV luminosity of this galaxy could be underestimated as the intrinsic UV emission may be higher than what is observed. This underestimation could lead to an overestimation of the ξ_{ion} .

4.3.2. SFR surface density

As mentioned in the introduction, the hydrogen density is approximately the electron density of an ionized gas. Some studies have suggested that the increased electron densities in high-redshift galaxies could be a major factor contributing to the increase in the ionization parameter (Davies et al. 2021; Reddy et al. 2023b,a). It is important to note that the electron densities from these studies are derived from $[\text{S II}] \lambda\lambda 6717, 6731$ or $[\text{O II}] \lambda\lambda 3727, 3729$, which measures the density in the low-ionization zone. This may differ from the density in higher ionization zones and the average electron density (Berg et al. 2021).

However, we do not have measurements of the electron density. Some studies have found a significant correlation between electron density and SFR *surface density* for galaxies at $z \sim 2$ (Shimakawa et al. 2015; Reddy et al. 2023b). These are related because the n_e of H II regions is governed by the molecular gas density and the balance between stellar feedback and ambient pressure (e.g., Davies et al. 2021), and the molecular gas density is related to the SFR *surface density* via the Kennicutt–Schmidt relation (e.g., Kennicutt et al. 2007; de los Reyes & Kennicutt 2019; Bacchini et al. 2019; Pessa et al. 2021). Here, we investigate whether the SFR surface density is correlated with O_{32} , and whether it affects the ionization parameter.

We derive the SFR surface density as:

$$\Sigma_{\text{SFR}} = \frac{\text{SFR}}{2\pi r_{\text{eff}}^2} [\text{M}_{\odot} \text{yr}^{-1} \text{kpc}^{-2}], \quad (12)$$

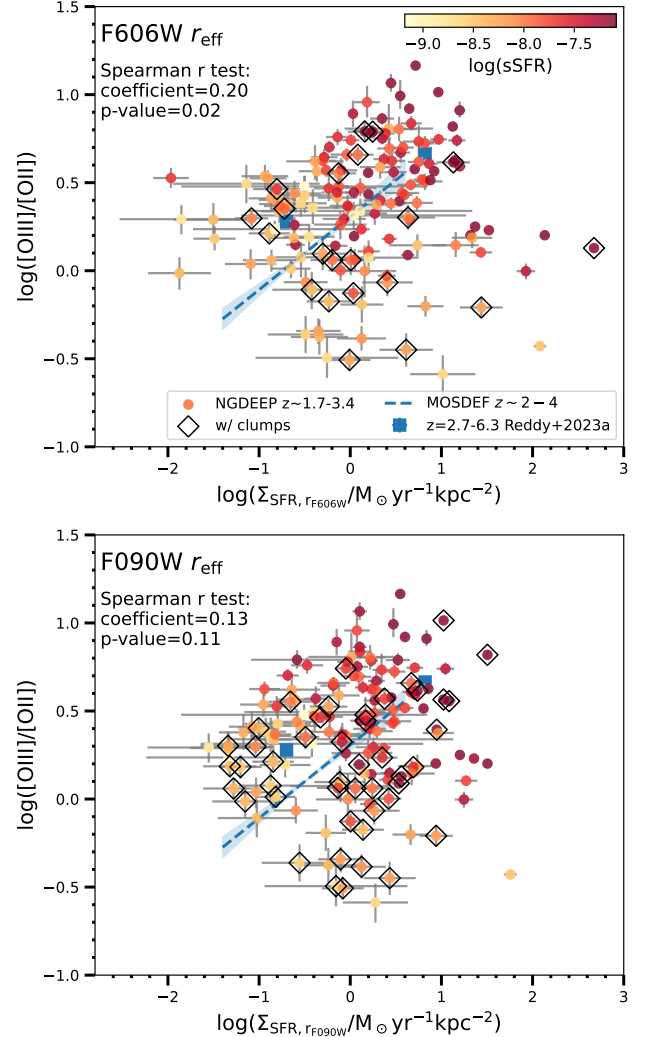


Figure 14. The distribution of the O_{32} ratio and Σ_{SFR} values for the NGDEEP final sample using effective radius measured from the HST F606W (*top*) and JWST F090W images (*bottom*). The data points are color-coded by sSFR . For galaxies identified with more than one component, we use the effective radius of the brightest clump. Such galaxies are marked with open black diamonds. In both panels, the median values of galaxies at $z = 2.7 - 6.3$ from Reddy et al. (2023a) are shown as blue squares, and the fit for MOSDEF galaxies at $z \sim 2 - 4$ (Reddy et al. 2023b) are shown as a blue dotted line. The SFR surface density may contribute to affecting O_{32} , but with a considerable scatter and sensitivity to the bandpass used for size measurements.

where r_{eff} is the effective radius of galaxies in units of kpc. For each galaxy, we estimate r_{eff} using two different bandpasses. We used both the *HST* F606W image and *JWST*/NIRCAM F090W images, and measured the effective radii with the PYSERSIC code (Pasha & Miller 2023). Because the SFR is derived from SED fitting which mostly relies on far-UV luminosity, we chose the

HST F606W image as this corresponds to rest-frame wavelengths of $\simeq 1400\text{--}2250 \text{ \AA}$. However, even though the F090W covers a less ideal set of rest-frame wavelengths $2050\text{--}3200 \text{ \AA}$, it provides better spatial resolution and deeper sensitivity, which is particularly important for measuring the size of small, low-mass galaxies. For the F606W sizes, we run PYSERSIC with a $2'' \times 2''$ cutout centered on the source with the image in a 60 mas scale, a PSF adopted from Finkelstein et al. (2022), and priors from SEP (Bertin & Arnouts 1996; Barbary et al. 2016) with a detection threshold of $5\times$ the RMS noise and a MINAREA of 5 pixels. We perform the PYSERSIC on F090W with the same setup, but with the image in a 30 mas scale and the PSF from WEBBPSF. For galaxies identified with more than one component in the segmentation, we use the effective radius of the brightest clump.

Figure 14 shows the distribution of O_{32} and Σ_{SFR} based on effective radius measured in F606W and F090W on the top and bottom panels, respectively. We find a significant correlation between O_{32} and Σ_{SFR} when using F606W r_{eff} , with a Spearman correlation coefficient of 0.20 and a p-value of 0.02. No correlation is found between O_{32} and Σ_{SFR} when using F090W r_{eff} with a p-value of 0.11. As a comparison, we show the fitted relation for MOSDEF galaxies at $z \sim 1.9\text{--}3.7$ derived by Reddy et al. (2023b) and the median values of galaxies at $z = 2.7\text{--}6.3$ from Reddy et al. (2023a). Our galaxies are scattered around the fitted relation from MOSDEF galaxies with a relatively large scatter of ~ 0.45 dex in both panels. Several potential factors could lead to the difference. Firstly, 18% and 31% of our galaxies show multiple components in the F606W and F090W images, respectively. As mentioned above, for galaxies with multiple detected clumps, we use only the effective radius of the brightest clump, which could underestimate the size of these galaxies and lead to an increase in the Σ_{SFR} . This effect is likely more pronounced in F090W, as more galaxies are spatially resolved into multiple components in this band. In addition, dust could bias our UV size measurements by artificially increasing the apparent size in UV when dust obscuration dominates in the central region of the galaxy (see further discussion in Shen et al. 2023). This effect is likely negligible in low-mass, high-sSFR galaxies in our sample as they have lower dust content and small $E(B - V)$. Another possible reason is that different data is used for size measurements. MOSDEF used the size measured from F160W, where light is dominated by an older stellar population. Meanwhile, the PSF of F160W is larger than F606W and F090W, which could bias the size of compact galaxies. Overall, we argue that the SFR sur-

face density may influence O_{32} , but with a considerable scatter and sensitivity to the bandpass used for size measurements.

Instead of using SFR from SED fitting and UV size, we can directly use $H\alpha$ emission line map to obtain a Σ_{SFR} map. This method is more straightforward and $H\alpha$ is less affected by dust compared with UV. In fact, we see evidence of a positive relation between O_{32} and Σ_{SFR} from the O_{32} ratio maps and $H\alpha$ -derived Σ_{SFR} maps. We will fully explore this in the next paper (Shen et al. in prep).

4.3.3. Density-bounded nebulae

In equation 9, we assumed a radiation-bounded nebula, where all ionizing photons are absorbed and converted to nebular emission. Alternatively, in the case of “density-bounded” nebulae, ionizing photons can escape. This can elevate the O_{32} ratio as the low-ionization region (where most of the $[O \text{ II}]$ originates) is not fully formed (see Nakajima & Ouchi 2014). Studies of low-redshift galaxies find that the O_{32} ratio correlates with the escape fraction H-ionizing photons, f_{esc} (Chisholm et al. 2018; Izotov et al. 2018). However, more recent studies suggest that a high O_{32} ratio may be a necessary but not sufficient condition for the large escape fraction (Nakajima et al. 2020; Choustikov et al. 2024). Future direct measurements of the escape fraction for our sample would allow us to test this. This study may be achievable using existing data from UVUDF (Teplitz et al. 2013; Rafelski et al. 2015), which covers rest-frame far-UV continuum at wavelengths $< 912 \text{ \AA}$. We will explore this in future work.

5. SUMMARY

We study the relation between O_{32} ratios and galaxy properties for 177 SFGs at $1.7 < z < 3.4$ using NIRISS slitless spectroscopy observations from the NGDEEP survey. The O_{32} ratio primarily traces the ionization parameter of the ISM, with a secondary dependence on metallicity. Our sample is selected based on the deep NIRISS spectra, primarily relying on the $[O \text{ III}]$ emission lines. All galaxies lie above the star-formation main sequence and span a stellar mass range of $10^7 - 10^{10.2} M_{\odot}$. Galaxy properties are estimated with ancillary deep HST and JWST imaging from CANDELS, JADES, and JEMS. Our results are summarized as follows:

- We find significant correlations between the O_{32} ratios and galaxies properties such that the O_{32} ratio increases with decreasing stellar mass, decreasing SFR, increasing sSFR, and increasing EW of $H\alpha$ and $H\beta$.

- We find that the O_{32} ratio is primarily driven by ionization parameters with a secondary dependence on metallicity, consistent with previous observational results and photoionization models. This suggests that the ionization parameter has a similar dependence on galaxy properties as is found for O_{32} .
- Compared to local normal galaxies, galaxies at $z \sim 2 - 3$ have a higher O_{32} ratio at fixed stellar mass and SFR, suggesting higher ionization parameter and/or low metallicity in $z \sim 2 - 3$ galaxies.
- We find that $z \sim 2 - 3$ galaxies have comparable or lower O_{32} to that measured for extreme galaxies at $z \sim 0$ at the fixed stellar mass, SFR, sSFR and $H\alpha$ and $H\beta$ EW, indicating these extreme galaxies at $z \sim 0$ have similar to higher ionization parameter and similar to lower metallicity.
- Our NGDEEP sample spans a wide range of O_{32} and stellar mass, which helps bridge the gap between the local and the $z > 5$ universe. We find a clear evolutionary trend in O_{32} and $EW(H\beta)$ from $z \sim 0$ to $z \gtrsim 5$ such that higher redshift galaxies have higher O_{32} at fixed $EW(H\beta)$ and extend to higher $EW(H\beta)$.
- We investigate the possible physical mechanisms behind the relation between the ionization parameter and recent star formation activity. We find that the O_{32} ratio is significantly correlated with the ionizing production efficiency. Meanwhile, the SFR surface density may contribute to affecting O_{32} , but with a considerable scatter and sensitivity to the bandpass used for size measurements. We argue that both the enhanced recent star formation activity and SFR surface density could be the main contributors to the increase in O_{32} and the ionization parameter.

This paper demonstrates the capability of *JWST*/NIRISS slitless spectroscopy data to measure the nebular emission line for low-mass galaxies $\log(M_*/M_\odot) \sim 10^7 - 10^9$ at $z \sim 2 - 3$. This dataset enables us to constrain star formation, metallicity, ionization parameter, and dust content of entire galaxies, as well as their spatially resolved profiles. With the extended mass range of galaxies, this dataset can bridge the gap between the local and $z > 5$ universe, enabling us to constrain the evolutionary trends of key galaxies and ISM properties.

1 We acknowledge the hard work of our colleagues in the
 2 NGDEEP collaboration and everyone involved in the
 3 *JWST* mission. This work benefited from support from
 4 the George P. and Cynthia Woods Mitchell Institute for
 5 Fundamental Physics and Astronomy at Texas A&M
 6 University. CP thanks Marsha and Ralph Schilling for
 7 generous support of this research. This work is based on
 8 observations made with the NASA/ESA/CSA *JWST*.
 9 The data were obtained from the Mikulski Archive for
 10 Space Telescopes at the Space Telescope Science Insti-
 11 tute, which is operated by the Association of Universities
 12 for Research in Astronomy, Inc., under NASA contract
 13 NAS 5-03127 for *JWST*. These observations are asso-
 14 ciated with program #2079. Some/all the *JWST* data
 15 presented in this paper were obtained from the Mikul-
 16 ski Archive for Space Telescopes (MAST) at the Space
 17 Telescope Science Institute. The specific observations
 18 analyzed can be accessed via [Leung, Gene et al. \(2023\)](#),
 19 [Williams, Christina et al. \(2023\)](#) and [Rieke, Marcia et al. \(2023\)](#).
 20 JM is grateful to the Cosmic Dawn Center for
 21 the DAWN Fellowship.

Facilities: HST (ACS, WFC3), *JWST* (NIRCAM, NIRISS)

Software: The python packages *ASTROPY* ([Astropy Collaboration et al. 2013, 2018](#)), *MATPLOTLIB* ([Hunter 2007](#)), *NUMPY* ([van der Walt et al. 2011](#)), and *SCIPY* ([Virtanen et al. 2020](#)) were extensively used.

REFERENCES

- Astropy Collaboration, Robitaille, T. P., Tollerud, E. J., et al. 2013, *A&A*, 558, A33, doi: [10.1051/0004-6361/201322068](https://doi.org/10.1051/0004-6361/201322068)
- Astropy Collaboration, Price-Whelan, A. M., Sipőcz, B. M., et al. 2018, *AJ*, 156, 123, doi: [10.3847/1538-3881/aabc4f](https://doi.org/10.3847/1538-3881/aabc4f)
- Bacchini, C., Fraternali, F., Iorio, G., & Pezzulli, G. 2019, *A&A*, 622, A64, doi: [10.1051/0004-6361/201834382](https://doi.org/10.1051/0004-6361/201834382)
- Bagley, M. B., Finkelstein, S. L., Koekemoer, A. M., et al. 2022, arXiv e-prints, arXiv:2211.02495, <https://arxiv.org/abs/2211.02495>
- Baldwin, J. A., Phillips, M. M., & Terlevich, R. 1981, *PASP*, 93, 5, doi: [10.1086/130766](https://doi.org/10.1086/130766)

- Barbary, K., Boone, K., McCully, C., et al. 2016, *kbarbary/sep*: v1.0.0, v1.0.0, Zenodo, doi: [10.5281/zenodo.159035](https://doi.org/10.5281/zenodo.159035)
- Berg, D. A., Chisholm, J., Erb, D. K., et al. 2021, *ApJ*, 922, 170, doi: [10.3847/1538-4357/ac141b](https://doi.org/10.3847/1538-4357/ac141b)
- Berg, D. A., James, B. L., King, T., et al. 2022, *ApJS*, 261, 31, doi: [10.3847/1538-4365/ac6c03](https://doi.org/10.3847/1538-4365/ac6c03)
- Bertin, E., & Arnouts, S. 1996, *A&AS*, 117, 393, doi: [10.1051/aas:1996164](https://doi.org/10.1051/aas:1996164)
- Bian, F., Kewley, L. J., Dopita, M. A., & Juneau, S. 2016, *ApJ*, 822, 62, doi: [10.3847/0004-637X/822/2/62](https://doi.org/10.3847/0004-637X/822/2/62)
- Blanc, G. A., Kewley, L., Vogt, F. P. A., & Dopita, M. A. 2015, *ApJ*, 798, 99, doi: [10.1088/0004-637X/798/2/99](https://doi.org/10.1088/0004-637X/798/2/99)
- Boquien, M., Burgarella, D., Roehlly, Y., et al. 2019, *A&A*, 622, A103, doi: [10.1051/0004-6361/201834156](https://doi.org/10.1051/0004-6361/201834156)
- Brammer, G., & Matharu, J. 2021, *gbrammer/grizli*: Release 2021, 1.3.2, Zenodo, doi: [10.5281/zenodo.5012699](https://doi.org/10.5281/zenodo.5012699)
- Brinchmann, J., Charlot, S., White, S. D. M., et al. 2004, *MNRAS*, 351, 1151, doi: [10.1111/j.1365-2966.2004.07881.x](https://doi.org/10.1111/j.1365-2966.2004.07881.x)
- Bruzual, G., & Charlot, S. 2003, *MNRAS*, 344, 1000, doi: [10.1046/j.1365-8711.2003.06897.x](https://doi.org/10.1046/j.1365-8711.2003.06897.x)
- Calzetti, D., Armus, L., Bohlin, R. C., et al. 2000, *ApJ*, 533, 682, doi: [10.1086/308692](https://doi.org/10.1086/308692)
- Cardelli, J. A., Clayton, G. C., & Mathis, J. S. 1989, *ApJ*, 345, 245, doi: [10.1086/167900](https://doi.org/10.1086/167900)
- Chabrier, G. 2003, *PASP*, 115, 763, doi: [10.1086/376392](https://doi.org/10.1086/376392)
- Chisholm, J., Gazagnes, S., Schaerer, D., et al. 2018, *A&A*, 616, A30, doi: [10.1051/0004-6361/201832758](https://doi.org/10.1051/0004-6361/201832758)
- Choustikov, N., Katz, H., Saxena, A., et al. 2024, *MNRAS*, 529, 3751, doi: [10.1093/mnras/stae776](https://doi.org/10.1093/mnras/stae776)
- Conroy, C., & Gunn, J. E. 2010, *FSPS: Flexible Stellar Population Synthesis*, Astrophysics Source Code Library, record ascl:1010.043
- Cullen, F., Cirasuolo, M., McLure, R. J., Dunlop, J. S., & Bowler, R. A. A. 2014, *MNRAS*, 440, 2300, doi: [10.1093/mnras/stu443](https://doi.org/10.1093/mnras/stu443)
- Curti, M., Mannucci, F., Cresci, G., & Maiolino, R. 2020, *MNRAS*, 491, 944, doi: [10.1093/mnras/stz2910](https://doi.org/10.1093/mnras/stz2910)
- Curti, M., Maiolino, R., Curtis-Lake, E., et al. 2024, *A&A*, 684, A75, doi: [10.1051/0004-6361/202346698](https://doi.org/10.1051/0004-6361/202346698)
- Davies, R. L., Förster Schreiber, N. M., Genzel, R., et al. 2021, *ApJ*, 909, 78, doi: [10.3847/1538-4357/abd551](https://doi.org/10.3847/1538-4357/abd551)
- de los Reyes, M. A. C., & Kennicutt, Robert C., J. 2019, *ApJ*, 872, 16, doi: [10.3847/1538-4357/aafa82](https://doi.org/10.3847/1538-4357/aafa82)
- Dopita, M. A., & Sutherland, R. S. 1996, *ApJS*, 102, 161, doi: [10.1086/192255](https://doi.org/10.1086/192255)
- . 2003, *Astrophysics of the diffuse universe*, doi: [10.1007/978-3-662-05866-4](https://doi.org/10.1007/978-3-662-05866-4)
- Eisenstein, D. J., Willott, C., Alberts, S., et al. 2023, *arXiv e-prints*, arXiv:2306.02465, doi: [10.48550/arXiv.2306.02465](https://doi.org/10.48550/arXiv.2306.02465)
- Ellison, S. L., Patton, D. R., Simard, L., & McConnachie, A. W. 2008, *ApJL*, 672, L107, doi: [10.1086/527296](https://doi.org/10.1086/527296)
- Emami, N., Siana, B., Alavi, A., et al. 2020, *ApJ*, 895, 116, doi: [10.3847/1538-4357/ab8f97](https://doi.org/10.3847/1538-4357/ab8f97)
- Emami, N., Siana, B., Weisz, D. R., et al. 2019, *ApJ*, 881, 71, doi: [10.3847/1538-4357/ab211a](https://doi.org/10.3847/1538-4357/ab211a)
- Endsley, R., Stark, D. P., Chevallard, J., & Charlot, S. 2021, *MNRAS*, 500, 5229, doi: [10.1093/mnras/staa3370](https://doi.org/10.1093/mnras/staa3370)
- Erb, D. K., Steidel, C. C., Shapley, A. E., et al. 2006, *ApJ*, 647, 128, doi: [10.1086/505341](https://doi.org/10.1086/505341)
- Estrada-Carpenter, V., Papovich, C., Momcheva, I., et al. 2019, *ApJ*, 870, 133, doi: [10.3847/1538-4357/aaf22e](https://doi.org/10.3847/1538-4357/aaf22e)
- Faisst, A. L., Capak, P. L., Emami, N., Tacchella, S., & Larson, K. L. 2019, *ApJ*, 884, 133, doi: [10.3847/1538-4357/ab425b](https://doi.org/10.3847/1538-4357/ab425b)
- Faisst, A. L., Masters, D., Wang, Y., et al. 2018, *ApJ*, 855, 132, doi: [10.3847/1538-4357/aab1fc](https://doi.org/10.3847/1538-4357/aab1fc)
- Finkelstein, S. L., Bagley, M., Song, M., et al. 2022, *ApJ*, 928, 52, doi: [10.3847/1538-4357/ac3aed](https://doi.org/10.3847/1538-4357/ac3aed)
- Finkelstein, S. L., Leung, G. C. K., Bagley, M. B., et al. 2024, *ApJL*, 969, L2, doi: [10.3847/2041-8213/ad4495](https://doi.org/10.3847/2041-8213/ad4495)
- Fukugita, M., Ichikawa, T., Gunn, J. E., et al. 1996, *AJ*, 111, 1748, doi: [10.1086/117915](https://doi.org/10.1086/117915)
- Grogin, N. A., Kocevski, D. D., Faber, S. M., et al. 2011, *ApJS*, 197, 35, doi: [10.1088/0067-0049/197/2/35](https://doi.org/10.1088/0067-0049/197/2/35)
- Guo, Y., Rafelski, M., Faber, S. M., et al. 2016, *ApJ*, 833, 37, doi: [10.3847/1538-4357/833/1/37](https://doi.org/10.3847/1538-4357/833/1/37)
- Hu, W., Papovich, C., Dickinson, M., et al. 2024, *ApJ*, 971, 21, doi: [10.3847/1538-4357/ad5015](https://doi.org/10.3847/1538-4357/ad5015)
- Hunter, J. D. 2007, *Computing in Science and Engineering*, 9, 90, doi: [10.1109/MCSE.2007.55](https://doi.org/10.1109/MCSE.2007.55)
- Inoue, A. K. 2011, *MNRAS*, 415, 2920, doi: [10.1111/j.1365-2966.2011.18906.x](https://doi.org/10.1111/j.1365-2966.2011.18906.x)
- Izotov, Y. I., Worseck, G., Schaerer, D., et al. 2021, *MNRAS*, 503, 1734, doi: [10.1093/mnras/stab612](https://doi.org/10.1093/mnras/stab612)
- . 2018, *MNRAS*, 478, 4851, doi: [10.1093/mnras/sty1378](https://doi.org/10.1093/mnras/sty1378)
- Jones, T., Martin, C., & Cooper, M. C. 2015, *ApJ*, 813, 126, doi: [10.1088/0004-637X/813/2/126](https://doi.org/10.1088/0004-637X/813/2/126)
- Jung, I., Finkelstein, S. L., Arrabal Haro, P., et al. 2024, *ApJ*, 967, 73, doi: [10.3847/1538-4357/ad3913](https://doi.org/10.3847/1538-4357/ad3913)
- Kaasinen, M., Kewley, L., Bian, F., et al. 2018, *MNRAS*, 477, 5568, doi: [10.1093/mnras/sty1012](https://doi.org/10.1093/mnras/sty1012)
- Kashino, D., Silverman, J. D., Sanders, D., et al. 2019, *ApJS*, 241, 10, doi: [10.3847/1538-4365/ab06c4](https://doi.org/10.3847/1538-4365/ab06c4)
- Kauffmann, G., Heckman, T. M., Tremonti, C., et al. 2003, *MNRAS*, 346, 1055, doi: [10.1111/j.1365-2966.2003.07154.x](https://doi.org/10.1111/j.1365-2966.2003.07154.x)

- Kelly, B. C. 2007, *ApJ*, 665, 1489, doi: [10.1086/519947](https://doi.org/10.1086/519947)
- Kennicutt, Robert C., J., Calzetti, D., Walter, F., et al. 2007, *ApJ*, 671, 333, doi: [10.1086/522300](https://doi.org/10.1086/522300)
- Kennicutt, R. C., & Evans, N. J. 2012, *ARA&A*, 50, 531, doi: [10.1146/annurev-astro-081811-125610](https://doi.org/10.1146/annurev-astro-081811-125610)
- Kewley, L. J., & Dopita, M. A. 2002, *ApJS*, 142, 35, doi: [10.1086/341326](https://doi.org/10.1086/341326)
- Kewley, L. J., Dopita, M. A., Leitherer, C., et al. 2013, *ApJ*, 774, 100, doi: [10.1088/0004-637X/774/2/100](https://doi.org/10.1088/0004-637X/774/2/100)
- Kewley, L. J., Nicholls, D. C., Sutherland, R., et al. 2019a, *ApJ*, 880, 16, doi: [10.3847/1538-4357/ab16ed](https://doi.org/10.3847/1538-4357/ab16ed)
- Kewley, L. J., Nicholls, D. C., & Sutherland, R. S. 2019b, *ARA&A*, 57, 511, doi: [10.1146/annurev-astro-081817-051832](https://doi.org/10.1146/annurev-astro-081817-051832)
- Kewley, L. J., Zahid, H. J., Geller, M. J., et al. 2015, *ApJL*, 812, L20, doi: [10.1088/2041-8205/812/2/L20](https://doi.org/10.1088/2041-8205/812/2/L20)
- Koekemoer, A. M., Faber, S. M., Ferguson, H. C., et al. 2011, *ApJS*, 197, 36, doi: [10.1088/0067-0049/197/2/36](https://doi.org/10.1088/0067-0049/197/2/36)
- Kriek, M., Shapley, A. E., Reddy, N. A., et al. 2015, *ApJS*, 218, 15, doi: [10.1088/0067-0049/218/2/15](https://doi.org/10.1088/0067-0049/218/2/15)
- Kroupa, P. 2001, *MNRAS*, 322, 231, doi: [10.1046/j.1365-8711.2001.04022.x](https://doi.org/10.1046/j.1365-8711.2001.04022.x)
- Lara-López, M. A., Cepa, J., Bongiovanni, A., et al. 2010, *A&A*, 521, L53, doi: [10.1051/0004-6361/201014803](https://doi.org/10.1051/0004-6361/201014803)
- Leitherer, C., & Heckman, T. M. 1995, *ApJS*, 96, 9, doi: [10.1086/192112](https://doi.org/10.1086/192112)
- Leung, Gene, Finkelstein, Steven, Papovich, Casey, & Pirzkal, Norbert. 2023, NGDEEP Epoch 1 NIRC*am* imaging data, STS*ci*/MAST, doi: [10.17909/3S7H-8K54](https://doi.org/10.17909/3S7H-8K54)
- Lyu, J., Alberts, S., Rieke, G. H., & Rujopakarn, W. 2022, *ApJ*, 941, 191, doi: [10.3847/1538-4357/ac9e5d](https://doi.org/10.3847/1538-4357/ac9e5d)
- Madau, P., & Dickinson, M. 2014, *ARA&A*, 52, 415, doi: [10.1146/annurev-astro-081811-125615](https://doi.org/10.1146/annurev-astro-081811-125615)
- Maiolino, R., Nagao, T., Grazian, A., et al. 2008, *A&A*, 488, 463, doi: [10.1051/0004-6361:200809678](https://doi.org/10.1051/0004-6361:200809678)
- Mannucci, F., Cresci, G., Maiolino, R., Marconi, A., & Gnerucci, A. 2010, *MNRAS*, 408, 2115, doi: [10.1111/j.1365-2966.2010.17291.x](https://doi.org/10.1111/j.1365-2966.2010.17291.x)
- Matharu, J., Muzzin, A., Brammer, G. B., et al. 2021, *ApJ*, 923, 222, doi: [10.3847/1538-4357/ac26c3](https://doi.org/10.3847/1538-4357/ac26c3)
- Matharu, J., Muzzin, A., Sarrouh, G. T. E., et al. 2023, *ApJL*, 949, L11, doi: [10.3847/2041-8213/acd1db](https://doi.org/10.3847/2041-8213/acd1db)
- Mingozzi, M., Belfiore, F., Cresci, G., et al. 2020, *A&A*, 636, A42, doi: [10.1051/0004-6361/201937203](https://doi.org/10.1051/0004-6361/201937203)
- Nakajima, K., Ellis, R. S., Robertson, B. E., Tang, M., & Stark, D. P. 2020, *ApJ*, 889, 161, doi: [10.3847/1538-4357/ab6604](https://doi.org/10.3847/1538-4357/ab6604)
- Nakajima, K., & Ouchi, M. 2014, *MNRAS*, 442, 900, doi: [10.1093/mnras/stu902](https://doi.org/10.1093/mnras/stu902)
- Noiro, G., Desprez, G., Asada, Y., et al. 2023, *MNRAS*, 525, 1867, doi: [10.1093/mnras/stad1019](https://doi.org/10.1093/mnras/stad1019)
- Oke, J. B., & Gunn, J. E. 1983, *ApJ*, 266, 713, doi: [10.1086/160817](https://doi.org/10.1086/160817)
- Osterbrock, D. E., & Ferland, G. J. 2006, *Astrophysics of gaseous nebulae and active galactic nuclei*
- Papovich, C., Simons, R. C., Estrada-Carpenter, V., et al. 2022, *ApJ*, 937, 22, doi: [10.3847/1538-4357/ac8058](https://doi.org/10.3847/1538-4357/ac8058)
- Pasha, I., & Miller, T. B. 2023, *Journal of Open Source Software*, 8, 5703, doi: [10.21105/joss.05703](https://doi.org/10.21105/joss.05703)
- Pessa, I., Schinnerer, E., Belfiore, F., et al. 2021, *A&A*, 650, A134, doi: [10.1051/0004-6361/202140733](https://doi.org/10.1051/0004-6361/202140733)
- Pirzkal, N., Rothberg, B., Papovich, C., et al. 2023, *arXiv e-prints*, arXiv:2312.09972, doi: [10.48550/arXiv.2312.09972](https://doi.org/10.48550/arXiv.2312.09972)
- Planck Collaboration, Ade, P. A. R., Aghanim, N., et al. 2016, *A&A*, 594, A13, doi: [10.1051/0004-6361/201525830](https://doi.org/10.1051/0004-6361/201525830)
- Prieto-Lyon, G., Strait, V., Mason, C. A., et al. 2023, *A&A*, 672, A186, doi: [10.1051/0004-6361/202245532](https://doi.org/10.1051/0004-6361/202245532)
- Rafelski, M., Teplitz, H. I., Gardner, J. P., et al. 2015, *AJ*, 150, 31, doi: [10.1088/0004-6256/150/1/31](https://doi.org/10.1088/0004-6256/150/1/31)
- Reddy, N. A., Topping, M. W., Sanders, R. L., Shapley, A. E., & Brammer, G. 2023a, *ApJ*, 952, 167, doi: [10.3847/1538-4357/acd754](https://doi.org/10.3847/1538-4357/acd754)
- Reddy, N. A., Kriek, M., Shapley, A. E., et al. 2015, *ApJ*, 806, 259, doi: [10.1088/0004-637X/806/2/259](https://doi.org/10.1088/0004-637X/806/2/259)
- Reddy, N. A., Sanders, R. L., Shapley, A. E., et al. 2023b, *ApJ*, 951, 56, doi: [10.3847/1538-4357/acd0b1](https://doi.org/10.3847/1538-4357/acd0b1)
- Rieke, M., & the JADES Collaboration. 2023, *arXiv e-prints*, arXiv:2306.02466, doi: [10.48550/arXiv.2306.02466](https://doi.org/10.48550/arXiv.2306.02466)
- Rieke, Marcia, Robertson, Brant, Tacchella, Sandro, et al. 2023, Data from the JWST Advanced Deep Extragalactic Survey (JADES), STS*ci*/MAST, doi: [10.17909/8TDJ-8N28](https://doi.org/10.17909/8TDJ-8N28)
- Sanders, R. L., Shapley, A. E., Topping, M. W., Reddy, N. A., & Brammer, G. B. 2024, *ApJ*, 962, 24, doi: [10.3847/1538-4357/ad15fc](https://doi.org/10.3847/1538-4357/ad15fc)
- Sanders, R. L., Shapley, A. E., Kriek, M., et al. 2016, *ApJ*, 816, 23, doi: [10.3847/0004-637X/816/1/23](https://doi.org/10.3847/0004-637X/816/1/23)
- . 2018, *ApJ*, 858, 99, doi: [10.3847/1538-4357/aabcbd](https://doi.org/10.3847/1538-4357/aabcbd)
- Sanders, R. L., Shapley, A. E., Reddy, N. A., et al. 2020, *MNRAS*, 491, 1427, doi: [10.1093/mnras/stz3032](https://doi.org/10.1093/mnras/stz3032)
- Sanders, R. L., Shapley, A. E., Jones, T., et al. 2021, *ApJ*, 914, 19, doi: [10.3847/1538-4357/abf4c1](https://doi.org/10.3847/1538-4357/abf4c1)
- Shen, L., Papovich, C., Yang, G., et al. 2023, *ApJ*, 950, 7, doi: [10.3847/1538-4357/acc944](https://doi.org/10.3847/1538-4357/acc944)
- Shen, L., Papovich, C., Matharu, J., et al. 2024, *ApJL*, 963, L49, doi: [10.3847/2041-8213/ad28bd](https://doi.org/10.3847/2041-8213/ad28bd)

- Shimakawa, R., Kodama, T., Steidel, C. C., et al. 2015, MNRAS, 451, 1284, doi: [10.1093/mnras/stv915](https://doi.org/10.1093/mnras/stv915)
- Simons, R. C., Papovich, C., Momcheva, I., et al. 2021, ApJ, 923, 203, doi: [10.3847/1538-4357/ac28f4](https://doi.org/10.3847/1538-4357/ac28f4)
- Simons, R. C., Papovich, C., Momcheva, I. G., et al. 2023, ApJS, 266, 13, doi: [10.3847/1538-4365/acc517](https://doi.org/10.3847/1538-4365/acc517)
- Skelton, R. E., Whitaker, K. E., Momcheva, I. G., et al. 2014, ApJS, 214, 24, doi: [10.1088/0067-0049/214/2/24](https://doi.org/10.1088/0067-0049/214/2/24)
- Steidel, C. C., Rudie, G. C., Strom, A. L., et al. 2014, ApJ, 795, 165, doi: [10.1088/0004-637X/795/2/165](https://doi.org/10.1088/0004-637X/795/2/165)
- Strom, A. L., Steidel, C. C., Rudie, G. C., Trainor, R. F., & Pettini, M. 2018, ApJ, 868, 117, doi: [10.3847/1538-4357/aae1a5](https://doi.org/10.3847/1538-4357/aae1a5)
- Strom, A. L., Steidel, C. C., Rudie, G. C., et al. 2017, ApJ, 836, 164, doi: [10.3847/1538-4357/836/2/164](https://doi.org/10.3847/1538-4357/836/2/164)
- Sutherland, R. S., & Dopita, M. A. 1993, ApJS, 88, 253, doi: [10.1086/191823](https://doi.org/10.1086/191823)
- Tang, M., Stark, D. P., Chevallard, J., & Charlot, S. 2019, MNRAS, 489, 2572, doi: [10.1093/mnras/stz2236](https://doi.org/10.1093/mnras/stz2236)
- Teplitz, H. I., Rafelski, M., Kurczynski, P., et al. 2013, AJ, 146, 159, doi: [10.1088/0004-6256/146/6/159](https://doi.org/10.1088/0004-6256/146/6/159)
- Tomczak, A. R., Quadri, R. F., Tran, K.-V. H., et al. 2016, ApJ, 817, 118, doi: [10.3847/0004-637X/817/2/118](https://doi.org/10.3847/0004-637X/817/2/118)
- Topping, M. W., Shapley, A. E., Sanders, R. L., et al. 2021, MNRAS, 506, 1237, doi: [10.1093/mnras/stab1793](https://doi.org/10.1093/mnras/stab1793)
- Tremonti, C. A., Heckman, T. M., Kauffmann, G., et al. 2004, ApJ, 613, 898, doi: [10.1086/423264](https://doi.org/10.1086/423264)
- van der Walt, S., Colbert, S. C., & Varoquaux, G. 2011, Computing in Science and Engineering, 13, 22, doi: [10.1109/MCSE.2011.37](https://doi.org/10.1109/MCSE.2011.37)
- Virtanen, P., Gommers, R., Oliphant, T. E., et al. 2020, Nature Methods, 17, 261, doi: [10.1038/s41592-019-0686-2](https://doi.org/10.1038/s41592-019-0686-2)
- Wang, X., Jones, T., Vulcani, B., et al. 2022, ApJL, 938, L16, doi: [10.3847/2041-8213/ac959e](https://doi.org/10.3847/2041-8213/ac959e)
- Whitaker, K. E., Labbé, I., van Dokkum, P. G., et al. 2011, ApJ, 735, 86, doi: [10.1088/0004-637X/735/2/86](https://doi.org/10.1088/0004-637X/735/2/86)
- Whitaker, K. E., Franx, M., Leja, J., et al. 2014, ApJ, 795, 104, doi: [10.1088/0004-637X/795/2/104](https://doi.org/10.1088/0004-637X/795/2/104)
- Williams, C. C., Tacchella, S., Maseda, M. V., et al. 2023, arXiv e-prints, arXiv:2301.09780, doi: [10.48550/arXiv.2301.09780](https://doi.org/10.48550/arXiv.2301.09780)
- Williams, Christina, Tacchella, Sandro, & Maseda, Michael. 2023, Data from the JWST Extragalactic Medium-band Survey (JEMS), STScI/MAST, doi: [10.17909/FSC4-DT61](https://doi.org/10.17909/FSC4-DT61)
- Yang, G., Boquien, M., Buat, V., et al. 2020, MNRAS, 491, 740, doi: [10.1093/mnras/stz3001](https://doi.org/10.1093/mnras/stz3001)
- Yang, H., Malhotra, S., Rhoads, J. E., & Wang, J. 2017a, ApJ, 847, 38, doi: [10.3847/1538-4357/aa8809](https://doi.org/10.3847/1538-4357/aa8809)
- Yang, H., Malhotra, S., Gronke, M., et al. 2017b, ApJ, 844, 171, doi: [10.3847/1538-4357/aa7d4d](https://doi.org/10.3847/1538-4357/aa7d4d)
- Zahid, H. J., Dima, G. I., Kudritzki, R.-P., et al. 2014, ApJ, 791, 130, doi: [10.1088/0004-637X/791/2/130](https://doi.org/10.1088/0004-637X/791/2/130)
- Zahid, H. J., Kewley, L. J., & Bresolin, F. 2011, ApJ, 730, 137, doi: [10.1088/0004-637X/730/2/137](https://doi.org/10.1088/0004-637X/730/2/137)